

July 10, 2018

The MACHO Project: 45 Candidate Microlensing Events from the First Year Galactic Bulge Data

C. Alcock^{1,2}, R.A. Allsman³, T.S. Axelrod^{1,4}, D.P. Bennett^{1,2},
K.H. Cook^{1,2}, K.C. Freeman⁴, K. Griest^{2,5}, J. Guern^{2,5},
M.J. Lehner^{2,5}, S.L. Marshall^{2,6}, H.-S. Park¹, S. Perlmutter²,
B.A. Peterson⁴, M.R. Pratt^{2,6}, P.J. Quinn⁴, A.W. Rodgers⁴
C.W. Stubbs^{2,6,7}, W. Sutherland⁸
(The MACHO Collaboration)

1 : Lawrence Livermore National Laboratory, Livermore, CA 94550

2 : Center for Particle Astrophysics,
University of California, Berkeley, CA 94720

3 : Supercomputing Facility,
Australian National University, Canberra, A.C.T. 0200, Australia

4 : Mt. Stromlo and Siding Spring Observatories,
Australian National University, Weston, A.C.T. 2611, Australia

5 : Department of Physics, University of California, San Diego, CA 92093

6 : Department of Physics, University of California, Santa Barbara, CA 93106

7 : Departments of Astronomy and Physics,
University of Washington, Seattle, WA 98195

8 : Department of Physics, University of Oxford, Oxford OX1 3RH, U.K.

Subject headings: Microlensing; Galaxy - structure; Brown dwarfs

ABSTRACT

We report the detection of 45 candidate microlensing events in fields toward the Galactic bulge. These come from the analysis of 24 fields containing 12.6 million stars observed for 190 days in 1993. Many of these events are of extremely high signal to noise and are remarkable examples of gravitational microlensing. The distribution of peak magnifications is shown to be consistent with the microlensing interpretation of these events. Using a sub-sample of 1.3 million “Clump Giant” stars whose distance and detection efficiency are well known, we find 13 events and estimate the microlensing optical depth toward the Galactic Bulge as $\tau_{\text{bulge}} = 3.9_{-1.2}^{+1.8} \times 10^{-6}$ averaged over an area of ~ 12 square degrees centered at Galactic coordinates $\ell = 2.55^\circ$ and $b = -3.64^\circ$. This is similar to the value reported by the OGLE collaboration, and is marginally higher than current theoretical models for τ_{bulge} . The optical depth is also seen to increase significantly for decreasing $|b|$. These results demonstrate that obtaining large numbers of microlensing events toward the Galactic bulge is feasible, and that the study of such events will have important consequences for the structure of the Galaxy and its dark halo.

1. Introduction

The main goal of the MACHO project gravitational microlensing survey is to search for massive compact halo objects (Machos) in the Milky Way halo in the mass range 10^{-7} – $100 M_{\odot}$, and thus to determine the contribution of Machos to the mass of the Milky Way halo. This is most readily achieved by searching for microlensing towards the Magellanic Clouds (Paczynski 1986), where the microlensing rate from a Macho-dominated halo is expected to be much larger than that from known stars (e.g. Gould, Miralda-Escude & Bahcall 1994, Alcock *et al.* 1995d).

However, it was realised at an early stage in the project that the Galactic bulge is also a promising target for microlensing surveys, for several reasons: firstly, there is a “known” microlensing rate from dim stars in the galactic disk and bulge (Griest *et al.* 1991; Paczynski 1991). Since there was considerable scepticism that microlensing events could be detected, due to their rarity and the need to reject intrinsic variable stars, this provides a useful check on the experiments. Also, since the duration of a microlensing event is related to the mass of the lensing object, microlensing towards the bulge can provide estimates of the very low mass end of the stellar mass function, which is difficult to measure directly, and can also test for the controversial “disk dark matter” (e.g. Bahcall 1986; Kuijken & Gilmore 1989), which (if it exists) is very likely to be in baryonic form. For a dedicated search like the MACHO project, the Galactic bulge is also convenient from an observational standpoint as it is visible when the Magellanic Clouds are too low in the sky to observe.

When the first microlensing data from the Galactic bulge was analyzed, it was discovered that the microlensing optical depth toward the bulge was larger than expected (Alcock *et al.* 1995a, Udalski *et al.* 1994a) suggesting that the standard models of the Galaxy needed to be revised. In fact, one possible explanation of the large optical depth toward the bulge is that the mass of the Galactic disk and bulge in ordinary stars is large enough to account for almost all of the mass interior to the Sun. If true, this would imply that the Galactic halo must have a large core radius or perhaps a rather small total mass. Thus, contrary to expectations, microlensing toward the Galactic bulge seems likely to reveal information about the properties of the Galaxy that are important for determining the properties of the Galaxy’s dark halo.

In this paper, we present the results from the analysis of 1993 data from our 24 well sampled Galactic bulge fields. We have searched this data set for microlensing events and found 45 candidate microlensing events. In § 2 we review the basic physics and status of microlensing experiments, in § 3 we discuss our observations and photometric reductions, and in § 4 we discuss our automated search for microlensing events, and the resulting candidates. In § 5 we provide an outline of the Monte-Carlo simulations used to estimate our detection efficiencies. In § 6 we compare our observed distribution of peak magnifications with the theoretical expectations and show that it is consistent with the microlensing interpretation. In § 7 we make several estimates of the optical depth of microlensing and compare our results with predicted event rates from simple models of the galactic disk and bulge. In particular, we consider the subset of stars classified as clump giants and obtain estimates of the optical depth which are relatively free of systematic uncertainties. In § 8 we discuss the microlensing

event timescales, and in § 9 we discuss the implications of our observed microlensing of a couple of bright main sequence stars. In § 10 and § 11 we discuss the implications of these results for the composition of the Dark Halo and summarize our conclusions.

2. Microlensing

The principle behind microlensing surveys is simple: if a compact object (e.g. a Macho or faint star) passes very close to the line of sight to a background star, the gravitational field of the object deflects the starlight and produces multiple images of the source. In the case of perfect alignment, the source star will appear as an ‘Einstein ring’, with a radius, r_E in the lens plane defined by

$$\begin{aligned} r_E &= \sqrt{\frac{4GmLx(1-x)}{c^2}} \\ &= 2.85 \text{ AU} \sqrt{\left(\frac{m}{M_\odot}\right) \left(\frac{Lx(1-x)}{1 \text{ kpc}}\right)}, \end{aligned} \quad (2.1)$$

where m is the lens mass, L is the observer-star distance, and x is the ratio of the observer-lens and observer-star distances. In a realistic case of imperfect alignment, the star will appear as two small arcs. For the scales of interest here, the image separation is $\lesssim 0.001$ arcsec, and is far too small to be resolved; however, the multiple imaging results in an apparent amplification of the source (e.g. Refsdal 1964) by a factor

$$A = \frac{u^2 + 2}{u\sqrt{u^2 + 4}}, \quad (2.2)$$

where $u = b/r_E$ and b is the distance of the lens from the undeflected observer-star line. Since objects in the Galaxy are in relative motion, this amplification will be transient, with a duration $\hat{t} \equiv 2r_E/v_\perp$, where v_\perp is the transverse velocity of the lens relative to the (moving) line of sight. For lens masses between a Jupiter mass and a Solar mass, \hat{t} is between a few days and a few months for most Galactic populations.

The suggestion by Paczyński (1986) that microlensing could be used to search for brown dwarfs or Jupiters that might comprise the Galactic halo* served to generate great interest in this technique and eventually led to the microlensing survey projects which began a few years later (Alcock *et al.* 1993, Aubourg *et al.* 1993, Udalski *et al.* 1993).

The great challenge of microlensing searches is that the microlensing probability is very small when the lens is in our Galaxy. The “optical depth” τ to microlensing is defined as the probability that any given star is microlensed with impact parameter $u < 1$ (i.e. $A > 1.34$)

* A similar calculation was carried out by Petrou (1981), but was not published.

at any given time. Since $r_E \propto \sqrt{m}$, while (for a given mass density) the number density of lenses $\bar{n} \propto m^{-1}$, τ is independent of the mass function of the lenses, and is given by

$$\tau = \frac{4\pi G}{c^2} \int_0^L \rho_{lens}(l) \frac{l(L-l)}{L} dl, \quad (2.3)$$

where l is the distance to the lens, L is the distance to the source stars, and $\rho_{lens}(l)$ is the mass density of the lensing objects. One complication for the optical depth towards the Galactic Bulge is that the source stars are spread over a fairly large range of distances. In this case, one must also average the optical depth over the distribution of source star distances L .

To get an order of magnitude estimate of τ , let us substitute M_{Galaxy}/L^3 for ρ_{lens} and identify L with a ‘typical’ Galactic distance. Dropping all numerical factors, eq. (2.3) becomes $\tau \sim GM_{Galaxy}/Lc^2 \sim v_c^2/c^2 \approx 10^{-6}$ where v_c is the Galaxy’s rotation speed. (We have used the virial theorem, $GM_{Galaxy}/L \sim v_c^2$, to obtain this expression.) Thus, the optical depth for lensing by objects in our Galaxy is of order 10^{-6} as shown by Paczyński (1986).

Although this optical depth is much lower than the fraction of intrinsic variable stars ($\sim 0.3\%$), microlensing events have many strong signatures which differ from all currently known types of variable star. For microlensing events involving a single point source, single lens, and uniform motions, the events are symmetrical and achromatic, with a shape given by

$$A(t) = A(u(t))$$

$$u(t) = \left[u_{\min}^2 + \left(\frac{2(t - t_{\max})}{\hat{t}} \right)^2 \right]^{0.5}, \quad (2.4)$$

where $A(u)$ is given by eq. (2.2), and $A_{\max} = A(u_{\min})$. Since the optical depth is so low, only one event should occur in any given star. If many events are found, additional statistical tests can be applied: the events should have a known distribution of peak amplifications, they should be spread appropriately across the color magnitude diagram, and the event timescales and peak amplifications should be statistically independent.

To our knowledge, four groups have reported detections of candidate microlensing events. Our MACHO collaboration has reported four candidate events towards the LMC (Alcock *et al.* 1993, 1994, 1995d), while the EROS collaboration has reported two events towards the LMC (Aubourg *et al.* 1993). Towards the Galactic bulge the event totals are much larger: the OGLE collaboration reports a total of 12 events (Udalski *et al.* 1993, 1994a), and the DUO Collaboration has found about 10 events (Alard *et al.* 1995, private communication). We have previously reported 4 of the 45 events presented here (Alcock *et al.* 1995a), and our real-time “Alert” system has detected over 40 events toward the Galactic Bulge during 1995.[†]

[†] Current information on the MACHO Collaboration’s Alert events is maintained at the WWW site: <http://darkstar.astro.washington.edu>, while the OGLE collaboration maintains similar information at <http://sirius.astrowu.edu.pl/~ftp/ogle/ews.html>.

3. Observations and Photometric Reductions

The MACHO project has full-time use of the 1.27-meter telescope at Mount Stromlo Observatory, Australia from mid-1992 through 2000. The telescope was recommissioned especially for this project, and a computer-controlled pointing and drive system was installed. A system of corrective optics has been installed near the prime focus, giving a focal reduction to $f/3.9$ with a 1° diameter field of view. A dichroic beamsplitter and filters provide simultaneous images in two passbands, a ‘red’ band (approx. 6300–7600 Å) and a ‘blue’ band (approx. 4500–6300 Å). Two very large CCD cameras are employed at the two foci; each contains a 2×2 mosaic of 2048×2048 pixel Loral CCD imagers. One half of one of the red focal plane CCDs does not function. The pixel size is $15 \mu\text{m}$ which corresponds to $0.63''$ on the sky, giving a sky coverage of 0.72×0.72 degrees. Each chip has two read-out amplifiers, and the images are read out through a 16-channel system and written into dual-ported memory in the data acquisition computer. The readout time is 70 seconds per image, and the noise is ~ 10 electrons rms, with a gain of $\sim 1.9 e^-/\text{ADU}$; the images are written to disk and then saved on Exabyte tape. Details of the camera system are given by Stubbs *et al.* (1993) and Marshall *et al.* (1994).

Observations are obtained during all clear nights and partial nights, except for occasional gaps for telescope maintenance. The default exposure times are 300 seconds for LMC images, 600 sec for the SMC and 150 seconds for the bulge, so over 60 exposures are taken per clear night. As of 1995 August, over 35000 exposures have been taken with the system, of which about 60% are of the LMC, 10% of the SMC and 30% of the bulge. The images are taken at standard sky positions, of which we have defined 82 in the LMC, 21 in the SMC and 75 in the bulge[‡]

Because the primary goal of the MACHO project is to measure the density of Machos residing in the Galactic halo, observations of the LMC and SMC have been given priority, so the bulge is observed only when the LMC is at an elevation $\lesssim 25^\circ$. In the first season of bulge observations in 1993, we concentrated on observing a subset of our bulge fields which is relatively close to the Galactic plane. During much of the observing season, many of the bulge fields were observed twice per night to improve the sensitivity to short time-scale events.

In this paper, we consider **only** the 1993 data from 24 well-sampled bulge fields containing dual color lightcurves for 12.6 million stars. The 24 fields used for this analysis are Macho field numbers 101, 102, 103, 104, 105, 108, 109, 110, 111, 113, 114, 115, 118, 119, 120, 121, 124, 125, 128, 159, 161, 162, and 167. The positions of these fields are indicated in Figure 1. The observations analysed here comprise 2313 images, covering a time span of 189 days from 1993 February 27 to 1993 September 03. The mean number of exposures per field is $2313/24 = 96$ with a range from 54 to 165. This sampling varies quite substantially among our fields, since we usually observed the fields in a fixed order each night so that our “highest priority” fields were always observed even on partially clear nights, and were frequently observed twice per night.

[‡] Coordinates of the field centers are available on the WWW,
URL: <http://wwwmacho.anu.edu.au>

3.1. PHOTOMETRIC REDUCTIONS

Photometric measurements from these images are made with a special-purpose code known as SoDoPHOT (Bennett *et al.* 1996), derived from DoPHOT (Schechter *et al.* 1993). First, one image of each field with good seeing and dark sky is chosen as a ‘template image’. This is processed in a manner similar to a standard DoPHOT reduction except that after one color of the image has been reduced, the coordinates of the stars found in the first color are used as starting points for the positions of stars in the second color; this improves the star matching between colors. (The final positions of the matched stars are forced to be the same in both colors, after allowing for differential refraction.) This procedure provides a ‘template’ catalog of stellar positions and magnitudes for each field.

All other images are processed in ‘routine’ mode, which proceeds as follows. First the image is divided into 120 ‘chunks’ of $\sim 512 \times 512$ pixels, and for each chunk ~ 30 bright stars are located and matched with the template. These stars are used to determine an analytic fit to the point spread function, a coordinate transformation, and a photometric zero point relative to the template. Then, all the template stars are subtracted from the image using the model PSF and coordinate transformation, and noise is added to the variance estimate for each pixel to allow for errors in the subtraction. Next, photometric fitting is carried out for each star in descending order of brightness, by adding the analytic model of the star back to the subtracted frame and fitting a 2-parameter model of the stellar profile and sky background, with pixels weighted by inverse variance, while the model PSF and computed position of the star are kept fixed. When a star is found to vary significantly from its template magnitude, it and its neighbors undergo a second iteration of fitting. For each star, the estimated magnitude and error are determined, along with 6 other parameters measuring the object ‘type’, the χ^2_{PSF} of the PSF fit, the crowding, the weighted fractions of flux removed due to bad pixels (f_{mis}) and cosmic rays (f_{CR}), and the fitted sky value. The crowding parameter f_{CRD} is defined to be the ratio of the flux contributed by other stars over the flux contributed by the individual star to that star’s central pixel, in seeing 30% worse than the actual seeing. The photometric error estimate is the formal PSF fit error (as in DoPHOT) with a 1.4% systematic error added in quadrature. These routine reductions are completed by SoDoPHOT at a rate of approximately 1 million photometric measurements per hour on a Sparc-10. The set of photometric data points for each field are re-arranged into a time-series for each star, combined with other relevant information including the seeing and sky brightness, and then passed to an automated analysis to search for variable stars and microlensing candidates.

4. Event Detection

The analysis of microlensing survey data presents some unusual challenges. The microlensing signal that we seek to detect affects only a few stars per million while a few stars per thousand are intrinsically variable. The vast majority of these variable stars are of known types and do not remain at a constant brightness for long periods of time. These common types of variable stars are not easily confused with microlensing. However, there may exist unusual variable star types which do resemble microlensing events, and these would be an important background for the microlensing search. Because microlensing surveys are, by far, the largest scale searches for stellar variability to date, we should not expect to learn about possible microlensing-like variable stars except through our own data. This complicates microlensing event detection.

In a laboratory experiments, one typically deals with the background by modeling it and then either subtracting or fitting the background model to the data. In our case, however, the variable star background is not known well enough to be modeled. Instead, the background must be discovered and characterized using the same data set that we use to search for microlensing events. The situation is not as bad as one might think because the high amplification subset of the microlensing events have lightcurves (*e.g.* events 101-D and 108-D in Figure 3) that are qualitatively very different from any variable star ever observed. Nevertheless, the event detection procedure is somewhat subjective, and some care must be taken to avoid biasing the results during the event detection analysis. We have attempted to do this using a set of cuts that are either fairly simple or have been determined *a priori* based upon analysis of an independent data set. For this analysis, all cuts which did not involve the χ^2 of the microlensing fit have been determined *a priori* while the cuts involving the microlensing fit χ^2 have been adjusted to fit the characteristics of this data set and the variable star background seen toward the bulge. The number of events close to the cut boundaries is small (especially for the clump giant sub-sample), so the conclusions reached below do not depend on the cuts we have chosen.

The first stage of the microlensing search is to define the set of ‘acceptable’ data points, using the PSF chi square, crowding, missing pixel, and cosmic ray flags described above. We have investigated the relationship between these quality flags and apparent ‘bad’ measurements as follows: we defined a set of ‘non-variable’ stars using a robust χ^2 measure, which is designed to reject periodic variables while including stars with occasional discrepant data points. For these stars, we then examine the percentiles of the distribution of $\Delta m/\sigma$ for many distinct bins of each flag. As expected, data points with large values of the various flags generally show a significant non-gaussian tail of outliers; thus, we set the following cuts on the various flags so as to reject most such outliers: $f_{\text{CR}} < 0.001$, $f_{\text{mis}} < 0.004$, $f_{\text{CRD}} < 3.0$, and $\chi^2_{\text{PSF}}(\text{d.o.f.}) < 4.0$. For bright stars, the deficiencies of the analytic PSF model become apparent, and this means that we must turn off the cut on $\chi^2_{\text{PSF}}(\text{d.o.f.})$ for stars with more than 63,000 detected photoelectrons. Data points failing any of these cuts are marked as ‘suspect’; they are retained in the database, but are not used in the microlensing or variability searches.

We exclude the reddest 0.2% of stars with $V - R > 1.6$ from the microlensing search

as these are often long-period variables which nearly always trigger the fitting routine, and would dominate the overall number of triggers. Stars which are very close to a chip boundary or which have less than 7 simultaneous red-blue measurements are also removed from the microlensing search.

The microlensing search through the light curve database proceeds in three stages: first, the time-series are convolved with a set of microlensing lightcurve filters of durations 7, 15 and 30 days in order to search for peaks of any kind. Any lightcurve with a significant peak in any filter is tagged as a ‘level-1’ trigger; about 1% of the stars pass this trigger. For these level-1 lightcurves a 5-parameter fit to a microlensing event is made, where the parameters are the un-amplified red and blue fluxes f_{R0}, f_{B0} , the peak amplification A_{\max} , the time of peak amplification t_{\max} and the event timescale \hat{t} . Thus, the fitted flux of the star in each color is given by

$$\begin{aligned} f_B(t) &= f_{B0}A(u(t)), \\ f_R(t) &= f_{R0}A(u(t)), \end{aligned} \quad (4.1)$$

where $A(u)$ is given by eq. (2.2), and $A_{\max} = A(u_{\min})$. Following the fit, a set of statistics describing the significance level, goodness of fit, achromaticity, crowding, temporal coverage of the event, etc. are calculated. Events above a modest significance level are tagged as ‘level-1.5’ events and are output as ASCII files, along with their associated statistics; these level-1.5 candidates are then subjected to more rigorous selection criteria, which may be easily modified, to search for final ‘level-2’ microlensing candidates.

Out of the 12.6 million stars in this data set, 37,485 stars passed the level-1.5 criteria. The most important of the ‘level-2’ cuts are shown in Fig. 2. The x-axis of Fig. 2 is $\Delta\chi^2 \equiv \chi^2_{\text{const}} - \chi^2_{\text{ml}}$, the difference between the χ^2 values for the constant-flux fit and the microlensing fit, while the y-axis of Fig. 2 is $\chi^2_{\text{ml}}(\text{d.o.f.})$ which is the χ^2 per degree of freedom for the microlensing fit. The large number of events at low $\Delta\chi^2$ generally contain small bumps attributable to low-level systematic errors. More than 90% of these level 1.5 candidates are stars which are just barely resolved from their closest neighbor in our best seeing images. They have spurious lightcurve bumps between days 175 and 190 which corresponds to a period when the telescope was out of alignment slightly because of a mirror support problem which was later repaired. We believe that the cause of the spurious photometry was the failure of the elliptic PSF used by SoDoPHOT to fit an asymmetric PSF caused by the telescope misalignment. This failure would allow the photometry of stars with very close neighbors to be contaminated with unsubtracted flux from their neighbors.

The two cuts shown in Fig. 2 are $\Delta\chi^2/\chi^2_{\text{ml}}(\text{d.o.f.}) > 400$ and $\Delta\chi^2/[\chi^2_{\text{ml}}(\text{d.o.f.})]^2 > 200$, and they are sufficient to cut the list of 37,485 ‘level 1.5’ microlensing candidates down to 52. Additional cuts on crowding parameter ($\langle f_{CRD} \rangle < 1.67$), time coverage, and the χ^2 in the peak region ($\Delta\chi^2/\chi^2_{\text{peak}} < 200$) remove the 8 events indicated by squares to yield 42 candidate events which are summarized in Table 1. (Three additional microlensing candidates which do not pass our cuts are also included in Table 1.) Lightcurves of these events are shown in Fig. 3 along with the best fit theoretical microlensing lightcurves. Some noteworthy events are indicated with superscripts on the event ID number in Table 1. A

superscript ^c indicates that the source star is classified as a clump giant, a class that will assume a special role when we estimate the microlensing optical depth.

The fits presented in Figure 3 do not account for the possibility that the lensed star might be blended with one or more other stars in our images. In this case only a fraction of the flux of an object that our photometry code has identified as a star will actually be lensed. In principle, one could account for this by allowing for an unlensed source to be superimposed on the lensed source in the microlensing fit. We have chosen not to do this for a number of reasons. The main difficulty is that there is a near degeneracy in parameter space for blended point mass microlensing light curves. By decreasing the fraction of the source that is lensed as the peak amplitude and duration are increased, one can construct a family of light curves with very similar shapes. Also, the amount of blending typically depends on seeing which varies significantly between observations so that stars that are identified to be separate in good seeing images are blended in poor seeing. In this situation, the photometry code preferentially selects the brighter star of the blend to receive the additional flux when the seeing is poor and the change in brightness is small. This can systematically change the shapes of microlensing light curves and prevent a meaningful determination of the blend fraction for a microlensing event.

In practice, we find that allowing for blending in our microlensing fits yields physically unlikely solutions for a large fraction of our lensing events. This suggests that artifacts like the one mentioned above are influencing the fits. At present, we are developing a new photometry routine (in collaboration with P. Stetson) that will reduce many images of previously detected events simultaneously. This routine should avoid the sort of artefacts mentioned above, so we will re-examine the issue of blending when this improved photometry is available.

In the present paper, however, the reader should note that the $1-\sigma$ fit errors reported in Table 1 tend to underestimate the true uncertainties in these quantities. This is mostly due to blending, but correlated and non-Gaussian measurement errors probably also contribute to this.

4.1. MICROLENSING EVENTS

Table 1 lists 45 microlensing events which include the 42 events which passed all of our cuts and 3 events which have been selected by eye as likely microlensing events from a larger sample of events passing less restrictive cuts. One of these three events is the binary lens event first seen by the OGLE group (Udalski *et al.* 1994b). In addition, we have determined that 2 of the 42 events which have passed our cuts are probably not microlensing events, and these are not used in our subsequent analysis. We do, however, include the binary lens event in most of our analyses in order to partially compensate for the fact that the microlensing fits used for event detection do not allow for binary lenses.

Clearly, our candidate microlensing events span a wide range in quality; some are of remarkably high signal-to-noise (e.g. 101-B, 108-D, 118-B) while others are relatively unimpressive (e.g. 110-C, 114-C). This is just as expected due to the range of amplifications and

stellar magnitudes involved; we provide a detailed discussion of these distributions in §4.2 and §6.

A number of the events shown in Figure 3 warrant further discussion. Three events have best fit amplifications substantially higher than the highest measured point. For events 101-D and 124-B where the highest measurement has $A \approx 15$, it is probably true that the best peak amplification was significantly higher, but it is also possible that the light curve of these stars may deviate from the form given by eqs. (2.2) and (2.4) if $u(t)$ should become as small as the projected radius of the source star. This would cause the light curve to steepen near the peak and then flatten off more abruptly at the peak. Undersampled events with this type of light curve will often generate best fit peak amplifications which are substantially in excess of the highest measured amplification. If events like 101-D, 124-B, and 108-D had been discovered prior to peak amplification by our alert system (which only became operational in August, 1994), then we would have the opportunity to obtain photometry with much better time resolution. Photometry of high amplification events like these with better time resolution would enable us to measure or set an interesting limit on the projected Einstein ring radius by comparison with the radius of the source star. [This effect has now been detected in MACHO Alert 95-30, and will be discussed in a later paper].

Two of the events (104-C and 119-A) shown in Figure 3 exhibit exotic deviations of a different type. Event 104-C shows a “parallax” effect in which the motion of the earth has caused $u(t)$ to deviate from the uniform motion assumed in eq. (2.4). This results in a slight asymmetry of the lightcurve, causing deviations from the best fit symmetric light curve shown in Figure 3. By fitting this light curve with a model which takes the motion of the earth into account, we are able to obtain a very good fit and thereby measure the lens velocity projected to the solar position. Details of this analysis and its implications are discussed in Alcock *et al.* (1995e). The other ‘exotic’ event is 119-A, which is a spectacular example of microlensing by a binary lens. This event was first seen by OGLE as event OGLE#7 (Udalski *et al.* 1994b); our data has considerably better time coverage which strongly confirms their binary lens interpretation. In our data, the second caustic crossing is resolved which is the first time such an effect has been observed (Alcock *et al.* 1995f). Note that while event the parallax event (104-C) passes all our cuts, the binary lens event (119-A) does not and must be moved from level-1.5 to level-2 by hand. It is necessary to do this because we have not incorporated binary lens fitting into our analysis. These events will be discussed in more detail in subsequent papers.

The superscript ^f in Table 1 is used to indicate the two events which seem to be microlensing events upon inspection but which do not pass our final level-2 cuts. One of these is event 104-B which fails the cut on the average value of the crowding parameter. This cut is designed to help remove some of the spurious level-1.5 microlens triggers which are caused by the effects of asymmetric point spread functions on very crowded stars. Unfortunately, it also has the effect of removing one or two likely microlensing candidates such as 104-B. The other probable event that fails the final cuts is 111-B. This fails because the time of the fit peak occurs later than day 238.5, which is the latest time for which we have added simulated events in the Monte Carlo calculations used to estimate our detection efficiency, so we must exclude it from our subsequent analysis which relies upon the efficiency estimates.

Finally, there are two events (denoted in Table 1 with a ^Y) which pass the cuts, but which we believe are not actual microlensing events. Event 113-C is located very close ($\sim 1''$) to a bright, very red long period variable which appears to be in phase with the event 113-C light curve. The behavior of the crowding parameters in the 113-C light curve suggests that the variation seen is probably due to contaminating flux from the neighboring variable, and not to star 113-C. The other suspicious event is 121-B. This light curve appears to resemble the light curves of a few other stars which do not quite pass the cuts, in that it appears to have a larger amplification in our blue passband and is somewhat asymmetric. We feel that there is a reasonably high probability that this event is an intrinsic variable and not a microlensing event. These two events are not used in the subsequent analysis.

In addition to these stars, there are a few other microlensing candidates in Table 1 and Figure 3 which have rather low signal to noise and/or poor time coverage. Because the vast majority of events which pass our cuts appear to have strong microlensing signatures, it appears that the microlensing event ‘signal’ is higher than the ‘background’ of microlensing-like variable stars. Thus, it seems likely that most of the ‘low quality’ events are also microlensing. We would like to emphasize, however, that our principal conclusions do not depend on these ‘low quality’ events.

Our field 119 covers about the same area of sky as the 9 OGLE fields BW1–BW8 and BWC, so we should expect to have some events in common with the OGLE collaboration. Unfortunately, the majority of their events occurred in 1992, before we were taking data on the bulge, but we confirm that all 5 of their 1992 lensing candidates in our field 119 remained constant in our 1993 observing season. There are 2 OGLE candidates in Baade’s Window during 1993, and we have rediscovered both of them: our event 119-A is OGLE-7 mentioned above, and event 119-D is OGLE-1. A third event seen by OGLE in 1993 (OGLE-8) falls outside our fields. We have also discovered two new events in field 119, namely 119-B and 119-C: these do occur in the OGLE fields but were not found by OGLE. A comparison with the light curves of the other OGLE events suggests that these events occurred during gaps in the OGLE observing schedule, so we would not expect OGLE to have detected them. We emphasize that this does not cast doubt on any OGLE results, since such gaps are already accounted for in their efficiency analysis (Udalski *et al.* 1994a).

In the following sections, we use several different samples of events. The optical depth and timescale analyses use the sample of 41 events which includes all events except for 104-B, 111-B, 113-C and 121-B. (The events which fail the cuts or are likely to be due to photometry errors and stellar variability are excluded.) For the distribution of peak amplifications, events 104-B, 111-B, and 119-A (the binary lens event) are excluded leaving a sample of 42 events. A proper binary lens fit would be required before event 119-A could be included.

4.2. COLOR MAGNITUDE DIAGRAM

Figure 4 shows a color magnitude diagram showing the locations of the baseline colors and magnitudes for each of these 45 stars as well as 7% of the stars in $5' \times 5'$ regions containing each of these stars. The color bands used for the plot are

$$\begin{aligned} V_M &= 0.94v + 0.06r \\ R_M &= 0.32v + 0.68r \end{aligned} \quad (4.2)$$

where v and r are the MACHO instrumental passbands, and V_M and R_M are designed to approximate Johnson V and R. No correction has been made for extinction, so the diagram is smeared out by extinction along a direction that is parallel to the left face of the quadrilateral drawn on the diagram. This quadrilateral is the region which we select as the ‘clump giant’ region of the color magnitude diagram. This region is defined by:

$$\begin{aligned} 0.1076 V_M - 1.008 &\leq V_M - R_M \leq 1.6 \\ R_M &\leq 18.0 \\ V_M &\geq 16.0 \end{aligned} \quad (4.3)$$

The region that is really populated by genuine clump giants (core helium burning horizontal branch stars) is the heavily populated region of the diagram close to the diagonal left face of this region. We have extended this region to include giants somewhat redder than the clump giants themselves because these stars are also (mostly) located in the bulge, and we would want to include any events found in this area of the color magnitude diagram.

There are a few features in the distribution of events on the color magnitude diagram that are of particular interest. It is evident that the events are spread all over the heavily populated regions of the color magnitude diagram, and this is consistent with the hypothesis that a large fraction of the events are truly microlensing; other types of variable stars generally appear only in particular regions of the color magnitude diagram. It is also true that the microlensing events are not a representative sample of the color magnitude diagram as there is a much larger fraction of microlensing events among the bright red clump giant branch stars than among the much more numerous fainter stars. There are two reasons why we expect this to be the case. The first is that our microlensing detection efficiency is much larger for the brighter stars because their signal-to-noise is higher and because crowding problems are less severe for brighter stars. Another reason is that the stars in different regions of the color magnitude diagram do not have the same distribution of distances. For example, a likely explanation of why there are so many more events on the bright giant branch than on the main sequence is that the giants are expected to reside mostly in the Galactic bulge while the main sequence stars are expected to be mostly foreground stars in the disk. This would substantially lower the microlensing optical depth for the main sequence stars. We discuss this more in § 9.

Another location in the color magnitude diagram which seems to be somewhat over represented in the set of candidate lensing events are the very faint stars at the bottom of

the diagram. In particular, the three events 120-A, 159-B, and especially 110-C come from an extremely sparse region at the bottom of the color magnitude diagram. There are several possible explanation for this. One very important contribution is amplification bias. Star 159-B was amplified by about 1.9 magnitudes in the template observation, and star 110-C was amplified by 0.9 magnitudes. Star 110-C probably would not have been above the detection threshold in the template if it had not been amplified, but star 159-B probably would have since it is in one of our less crowded bulge fields. Also, event 120-A and particularly event 110-C are rather low signal-to-noise, it is possible that one or both of these events are due to stellar variability rather than microlensing. A final possibility to be considered is that some of these faint stars may be significantly behind the bulge where the optical depth to microlensing would be much higher.

5. Microlensing Detection Efficiency

Before we can draw any conclusions about the statistical properties of the detected microlensing events, we need to assess our microlensing detection efficiency. There are a number of effects that influence our detection efficiency, and we separate them into two different classes which we refer to as the sampling efficiency, \mathcal{E}_s , and the blend efficiency, \mathcal{E}_b . The detection probability for a single event is a function of the event timescale \hat{t} , the stellar magnitude, the peak amplification and the peak time, but we can average over the latter 3 parameters using the known distributions, giving our efficiencies as a function only of event timescale $\mathcal{E}_s(\hat{t}), \mathcal{E}_b(\hat{t})$.

The sampling efficiency, $\mathcal{E}_s(\hat{t})$, is defined as the fraction of microlensing events in all monitored stars with $A_{\max} > 1.34$ which we expect to detect, taking into account the actual spacing of the observations, the variable seeing and sky brightness, as well as our event selection criteria. The sampling efficiency is calculated by adding a single simulated microlensing event to a random 1% of all stars, with a uniform distribution in $\log \hat{t}$ for $0 \leq \log_{10}(\hat{t}/\text{days}) \leq 2.5$, and uniform distributions in u_{\min} and t_{\max} . For each event and each data point, we add the excess flux given by $(A(t)-1)f_{\text{med}}$ to the observed flux, where A is the theoretical amplification, and f_{med} is the median observed flux of the star; this preserves the “real” scatter in the data points. We then search this ‘simulated event’ lightcurve database using the same procedure as in the actual lightcurve database, and $\mathcal{E}_s(\hat{t})$ is defined as the fraction of events with time scale \hat{t} that are recovered. Thus, the sampling efficiency takes into account events that are missed because of imperfect time sampling, periods of poor photometry due to bad seeing or a bright sky background, or just because they fail some of the cuts on crowding, color, etc. This method implicitly assumes the database contains photometry of single (unblended) stars, and that the photometric errors are well characterized by the error estimates that are generated by the photometry code. Figure 5 shows the sampling efficiencies for all our stars, and for only the stars falling within the clump giant region of the color magnitude diagram (Figure 4).

In the crowded stellar fields that are surveyed for microlensing events, the blending of overlapping stellar images causes many of the fainter stars not to be identified as individual stars. Furthermore, since the positions of the blended stars do not, in general, exactly

coincide, the blending effects will depend on seeing. Blending makes it more difficult to detect microlensing events because the blend of multiple stars is amplified by a smaller amount than the lensed star itself. Of course, one also has a chance to detect lensing of the other members of the blend, which can partially counteract the decrease in sensitivity caused by the blending, but it can be shown that a microlensing search is the most sensitive in the case where all the detected stars are actually unblended single stars.

We refer to the efficiency calculated with the effects of blending taken into account as the blend efficiency, \mathcal{E}_b . This is properly determined by adding “artificial” stars with the same luminosity function as the real stars to the raw images. The brightnesses of these artificial stars can be modulated according to randomly selected microlensing light curves, and then the analysis can be run to see how many of these simulated events are recovered. To date, the MACHO collaboration has calculated blend efficiencies only for our first year LMC data analysis (Alcock *et al.* 1995c, 1995d). There, we find that the effect of blending is to reduce $\mathcal{E}_b(\hat{t})$ to be 20–40% less than $\mathcal{E}_s(\hat{t})$ depending on \hat{t} . The bulge luminosity function is rather different from that of the LMC, and our bulge fields have an average stellar density some 30% higher than in the LMC. Thus, the ratio of blending to sampling efficiencies in the bulge may be somewhat different to that in the LMC, and we parameterize this by the uncertain factor $f_{blend} = \mathcal{E}_b/\mathcal{E}_s \sim 0.75$. In order to minimize this uncertainty, we will draw our main conclusions from the subset of ‘clump giant’ stars. These stars are much brighter than the typical stars in these fields, so significant blending is uncommon. Thus, the approximation $\mathcal{E}_b \simeq \mathcal{E}_s$ is a reasonable one for the ‘clump giants’.

One aspect of microlensing that we have not taken into account is the fact that the standard microlensing light curve used in our analysis and efficiency calculations does not describe all microlensing events. The parallax and binary lens events (104-C and 119-A) are clear illustrations of this fact. It is, of course, possible to include exotic events in the simulated event light curves used to estimate our efficiencies, but this involves assumptions about a number of new parameters that we have little information about. In the present paper, we make the (crude) assumption that our efficiency to detect exotic events is the same as our efficiency to detect events which follow the standard microlensing light curve. This causes us to overestimate our efficiency somewhat, but since these exotic events are rare this is not likely to be a large effect. This also justifies our inclusion of event 119-A in our microlensing candidate list despite the fact that it did not pass our cuts. Such a spectacular event would certainly pass any reasonable set of cuts that takes binary events into account, so we clearly need to include it to reduce the “exotic event” error in our efficiency estimates. We should also point out that this crude treatment of exotic lensing events clearly implies that we can make no meaningful statements about the fraction of binary lenses toward the Galactic bulge based upon the current analysis. We plan to address this point in a future publication after we have completed a more comprehensive study of our detection efficiencies.

6. Distribution of Peak Amplifications

One important test of the microlensing hypothesis is that the distribution of peak amplifications should follow the theoretical prediction that actual events should be uniformly distributed in u_{\min} . In order to compare with the distribution of detected events, we must include the fact that the detection efficiency depends on u_{\min} . Ideally, we should use the full blend efficiencies in the comparison of the u_{\min} distribution, but as we have stated, these efficiencies are not yet available (except for the subset of clump giant events where we have argued that the full efficiency equals the sampling efficiency to a good approximation). In what follows we test the microlensing hypothesis using sampling efficiencies both for our entire sample of microlensing events and for the clump giant sub-sample.

The Kolmogorov-Smirnov (or K-S) test is a convenient statistical test to compare the predicted and observed u_{\min} distributions. We will compare the predicted to the observed u_{\min} distribution for the set of 42 events which pass our cuts. (The binary lens is *not* included in this comparison.) In order to correct the u_{\min} distribution for the sampling efficiency, we want to average our calculated sampling efficiency $\mathcal{E}_s(u_{\min}, \hat{t})$ over the underlying \hat{t} distribution. An approximation to the actual \hat{t} distribution can be calculated by taking the observed \hat{t} distribution and weighting each event by the inverse of its detection efficiency. Averaging over this distribution gives the u_{\min} distribution we should expect in our observed data, given that the actual u_{\min} distribution should be uniform.

The cumulative distribution functions are shown in Figure 6(a), where the solid line shows the efficiency corrected theoretical distribution. The K-S statistic is 0.13 which gives $P_{KS} = 0.41$. We also compare to the uncorrected theoretical distribution (the dashed line). This curve is shown to indicate the effect of the sampling efficiencies on the u_{\min} distribution. Since the difference between the full blend efficiency ($\mathcal{E}_b(\hat{t})$) and the sampling efficiency ($\mathcal{E}_s(\hat{t})$) is much smaller than the difference between $\mathcal{E}_s(\hat{t})$ and $\mathcal{E}(\hat{t}) \equiv 1$, the comparison to the theoretical u_{\min} distribution corrected by $\mathcal{E}_s(\hat{t})$ is probably a reasonable test of the microlensing hypothesis. Thus we find good consistency with the hypothesis that our 42 events are due to microlensing (although, strictly speaking, it would be preferable to do this test with full blend efficiencies).

Finally, we should also compare the u_{\min} distribution for the 13 clump giant events with the theoretical distribution modified by the sampling efficiency because this is the set of events which we use to draw our conclusions regarding the microlensing optical depth toward the Bulge. For these 13 events (shown in Figure 6(b)) we find a K-S statistic of .046 which yields $P_{KS} = 0.31$. Thus, this data subset is also consistent with the microlensing prediction of a uniform u_{\min} distribution.

7. Optical Depth Estimates

The results of a gravitational microlensing experiment can be described in terms of the optical depth, τ , or the detected event rate, Γ , along with the set of event timescales. The optical depth is a measure of the mass in microlensing objects along the line of sight to the source stars, and it has the virtue that it is independent of the mass of the lensing objects as long as those masses generate events which fall within our region of sensitivity. Thus, one can compare predictions and measurements of τ using models of galactic mass distributions, without requiring details of the mass functions and velocity distributions of the microlensing objects. Then, for models which can match the observed optical depth, one can compare more detailed mass functions and velocity distributions with the set of observed event timescales, $\{\hat{t}_i\}$.

Experimentally, one can define an estimated optical depth as the observed microlensing rate times the efficiency weighted average event duration:

$$\tau_{\text{est}} = \frac{\pi}{4E} \sum_i \frac{\hat{t}_i}{\mathcal{E}(\hat{t}_i)}, \quad (7.1)$$

where E is the total exposure (in star-years), \hat{t}_i is the fit Einstein ring diameter crossing time for the i -th event, and $\mathcal{E}(\hat{t}_i)$ is the detection efficiency as a function of \hat{t} .

One difficulty with using the optical depth rather than the event rate to quantify the ‘amount’ of microlensing is that since each event contributes a different amount to the optical depth (eq. (7.1)), the uncertainty in the optical depth does not follow Poisson statistics. However, since the number of events still obeys Poisson statistics, it is straight forward to evaluate confidence level limits using Monte Carlo simulations in which the number of events for each simulated experiment is selected according to Poisson statistics. In order to calculate the optical depth for a given simulation, each simulated event must also be assigned a timescale, \hat{t}_i . The timescales are selected randomly from an assumed distribution of event timescales. If the number of detected events, N , is large, one can simply use the observed set of event timescales, $\{\hat{t}_i\}$. However, because both the mean and variance are measured from the same dataset, this procedure will underestimate the variance of the timescale distribution by a factor of $(N - 1)/N$. Nevertheless, we shall use this procedure for estimating the error bars in the present paper because it less dependent on theoretical models. The reader should be warned that the optical depth errors are being underestimated for data subsets with small numbers of events.

The ‘raw’ bulge optical depth estimated for our full sample using sampling efficiencies $\mathcal{E}_s(\hat{t})$ is $\tau_{\text{all,raw}} = 1.46 \times 10^{-6}$. (The full sample includes 41 events: the 43 which pass the cuts minus the 2 events which are probably not microlensing.) However, this value for τ is almost certainly an underestimate because of blending effects, and the fact that some fraction of the source stars are foreground stars in the foreground disk for which the optical depth is considerably lower. As we have discussed above, the use of sampling efficiencies is a rather poor approximation for the fainter stars in the sample. Toward the LMC, we found that the ratio of the full efficiencies to the sampling efficiencies was $\mathcal{E}_b(\hat{t})/\mathcal{E}_s(\hat{t}) \approx 0.66\text{--}0.8$ depending

on \hat{t} . Toward the bulge, this difference might be larger because the average stellar density is higher, and we are detecting more photons from the faintest stars we can identify toward the bulge. (Our limiting magnitude is determined by crowding.) This means that crowding-related systematic errors will be larger relative to the random errors in the bulge. We are undertaking a “full” efficiency analysis similar to that for the LMC, but for the present we just apply a crude correction factor of f_{Blend}^{-1} where we estimate $f_{\text{Blend}} \sim \langle \mathcal{E}_B(\hat{t}) \rangle / \langle \mathcal{E}_S(\hat{t}) \rangle \approx 0.75$.

The second important effect that will lower our raw τ value is that a significant fraction of the stars seen in these fields are probably foreground disk stars for which the microlensing optical depth would be lower. In principle, we could also have background disk stars which would have a higher optical depth, but our lines of sight toward the Bulge are several hundred parsecs out of the Galactic plane on the far side of the Bulge. Also, in the very crowded fields we have observed, we expect that most of the disk ‘contamination’ will be from foreground stars. As we will see in the next section, there is some independent evidence that the source stars for clump giant and ‘non-clump giant’ events come from different populations as the timescale distributions of the two samples are significantly different from one another. The fraction of disk stars in our fields is rather uncertain, but Minniti (1995) estimates from the DIRBE maps of Weiland *et al.* (1994) that the disk contributes 15% of the integrated 2.2 micron flux from Baade’s Window. Since our magnitude limit is fainter than the base of the giant branch, most of the optical flux should be resolved into stars in our data. Since the disk stars are on average bluer and will suffer less extinction, the fraction of disk stars in our optical passbands is probably larger than their fractional contribution to the 2.2 micron flux; thus we adopt a conservative estimate $f_{\text{Disk}} \approx 0.2$, and then correct our estimated optical depth by a factor of $(1 - f_{\text{Disk}})^{-1}$.

Then, our corrected estimate for the optical depth for bulge stars using our full sample of 41 events is $\tau_{\text{all,cor}} \approx 2.4 \pm 0.5 \times 10^{-6} (0.75/f_{\text{Blend}}) (0.8/(1 - f_{\text{Disk}}))$, where the latter two factors are somewhat uncertain but should be fairly close to 1.

7.1. OPTICAL DEPTH FOR CLUMP GIANTS

As we have seen above, there are significant uncertainties in our estimated bulge optical depth from the full sample, both due to blending and the fact that some of the stars seen towards the galactic bulge are foreground disk stars. One way to avoid both these problems is to concentrate on a class of stars that is both bright and ‘known’ to be in the galactic bulge: the ‘clump giant’ stars. These are relatively low mass core helium burning giants—the horizontal branch of a metal rich population, and this is the same population used by the OGLE collaboration (Stanek *et al.* 1994; Paczyński *et al.* 1994) to find evidence for a Galactic bar in their data. The location of the clump giants is marked on the color magnitude diagram in Figure 4. Note that due to the variable extinction across our fields, the position of the giant clump is spread out in the color magnitude diagram shown in Figure 4, but fortunately the clump stars still occupy a distinct region of the color magnitude diagram.

Table 2 shows our estimated optical depths and various confidence level limits for a number of different cuts on the data. As mentioned above, it is the ‘clump giant’ values that are the most reliable measurements of the optical depth toward stars in the bulge. Thus,

our estimated optical depth toward the clump giants[†] averaged over all our fields is $\tau_{\text{CG}} = 3.9_{-1.2}^{+1.8} \times 10^{-6}$. This is somewhat higher, but only at the $\sim 1\sigma$ level, than the corrected optical depth for all stars estimated above: $\tau_{\text{all,cor}} \approx 2.4 \pm 0.5 \times 10^{-6} (0.75/f_{\text{Blend}})(0.8/(1-f_{\text{Disk}})$.

There are several factors that could contribute to this difference. First, it could be that $f_{\text{Blend}} < 0.75$ or $f_{\text{Disk}} > 0.2$ since our estimates of these values are very rough. Another important consideration is that the number of stars observed across our fields is limited by crowding for the full sample but not for the clump giant sample. This means that the number density of stars in the full sample does not vary much across the sky while the density of clump giants varies by a factor of 6 across our fields. This is the reason that the average ℓ and b values for the two samples shown in Table 2 are different. Since the clump giants are more concentrated toward the Galactic center, we should expect a larger optical depth for this sample. We should also expect that the clump giants are systematically more distant than the full sample of bulge stars. Faint stars on the far side of the bulge are less likely to be detected because they appear fainter than similar stars on the near side of the bulge, but essentially all of the clump giants are bright enough to be in our sample, so the nearer ones are less favored. This effect also serves to increase the optical depth seen towards the clump giants. In any case, the difference in optical depth seen toward these two samples does not have a large statistical significance, and the implied 95% lower limits on the optical depth are quite similar for the two samples. We will use the clump giant sample for our main conclusions because the uncertainties are better understood for this sample.

7.2. OPTICAL DEPTH AS A FUNCTION OF LATITUDE

The third and fourth rows of Table 2 show τ_{bulge} for two different cuts on Galactic latitude: $|b| < 3.5^\circ$ and $|b| > 3.5^\circ$. Although, the majority of stars we have observed fall into the $|b| > 3.5^\circ$ category, the density of clump giants falls off quite rapidly away from the galactic plane and the observed population of clump giants is about evenly divided about $b = -3.5^\circ$. It was originally hoped that the variation of τ_{bulge} with galactic latitude might help to distinguish different Galactic models which seek to explain the observed microlensing optical depth toward the bulge. Certainly, the strong variation of τ with b is what one would expect from lensing by the disk, but unfortunately, the situation is not very different with models where the Galactic bar is the dominant source of lenses (Zhao *et al.* 1994; Han & Gould 1995a). Thus, the apparent variation of τ_{bulge} with b does not resolve the question as to whether the bulk of the lenses are in the Galactic disk or bar. We are continuing our observations and have extended our coverage in both Galactic latitude and longitude in order to obtain improved constraints on the latitude and longitude dependence of τ and the microlensing event rate: in particular, we are now monitoring a number of fields at $l \sim 10^\circ, b \sim -3^\circ$ where disk lensing is expected to dominate. We will present results of these investigations in a future publication.

[†] The τ for the clump giant sample differs from that in a previous paper (Bennett *et al.* 1995) because the clump giant cut used previously was too loose and included many stars which are not clump giants.

7.3. COMPARISON OF OPTICAL DEPTH WITH MODEL PREDICTIONS AND OTHER DATA

The predictions of the microlensing optical depth toward the Galactic bulge made prior to the first experimental estimates were in the range $\tau \approx 1 - 1.5 \times 10^{-6}$ (Griest *et al.* 1991; Paczyński 1991; Kiraga & Paczyński 1994) toward Baade's Window. This is about a factor of 3 below the best fit value $\tau_{CG} = 3.9 \times 10^{-6}$ reported here and below our 95% confidence level lower limit of 1.9×10^{-6} . We note that these values are averaged over ~ 10 square degrees centered at $\langle \ell \rangle = 2.55^\circ$ and $\langle b \rangle = -3.64^\circ$; this is close to but not the same as Baade's Window at $\langle \ell \rangle = 1.0^\circ$ and $\langle b \rangle = -3.9^\circ$. In most models, the optical depth averaged over our fields is very close to the optical depth at Baade's Window, so we ignore this distinction for the rest of this section.

The results presented here agree quite well with our previous result based on a subset of this data (Alcock *et al.* 1995a) and with the OGLE result of $\tau_{BW} \geq 3.3 \pm 1.2 \times 10^{-6}$ toward Baade's window (Udalski *et al.* 1994a). In comparing to this value, it is often not realized that this value is a *lower limit* on the optical depth because they have ignored blending effects when estimating their detection efficiencies. (The OGLE paper makes this point quite clearly.) Since they do not restrict themselves to a bright subset of stars, the blending correction may be substantial. For example, if their data and analysis were similar to our LMC data and analysis, then their estimated optical depth towards Baade's window would increase by a factor of ~ 1.25 when blending is taken into account. However, we should emphasize that the differences between our data sets and analysis methods might imply that the correction factor for OGLE would be quite different from this.

In response to the first optical depth estimates toward the bulge, a number of attempts have been made to produce models which can account for the microlensing seen toward the bulge. We (Alcock *et al.* 1995a) and Gould (1994) have suggested that the galactic disk might contain most of the Galactic mass interior to the solar circle. For a double exponential disk with any scale length and height, the optical depth toward the center of our fields is $\tau \lesssim 1.6 \times 10^{-6} (v_d/200 \text{ km/sec})^2$, where v_d is the circular velocity at the solar radius due to the disk. If we add the contribution, $\tau = 5 \times 10^{-7}$ due to a low mass axially symmetric bulge to the disk value for $v_d = 200 \text{ km/sec}$, then the total, $\tau = 2.1 \times 10^{-6}$ is formally ruled out by our data at the 93% confidence level. A more extreme set of models was considered by Gould who finds that $\tau \leq 3 \times 10^{-6}$ at Baade's window for any disk distribution with an exponential scale height and arbitrary radial profile. Thus, it is possible to have optical depths much closer to the measured value with a massive disk that does not follow the exponential density relation with radius.

Some have argued against the heavy disk models on the grounds that the measured column density of the disk may be as small as $50 \text{ M}_\odot \text{pc}^{-2}$ (Kuijken and Gilmore 1989) although this estimate is sensitive to the assumed model of the dark halo. Even if the assumed halo model is correct, however, one must also take the assumed exponential scale length dependence of the disk quite seriously in order to make any connection between the local column density and the global mass distribution of the disk. In fact, while the scaling of the average disk mass density with radius seems to be well fit by an exponential, the variation of the column density with galactic longitude seems to be quite significant: a factor of 2–3

in cases that have been studied in some detail (Rix & Zaritsky 1995, Gnedin, Goodman & Frei 1995, Rix & Rieke 1993). Thus, the apparently small local column density is not a serious objection to the heavy disk model. Recent estimates of the disk scale length which give values as small as 2.5 kpc (Fux & Martinet 1994) also tend to indicate that a large disk mass is compatible with the limits on the local disk column density.

Another type of model that has been proposed to explain the high optical depths seen toward the bulge is a Galactic bar with the long axis pointing close to the line of sight. The existence of a bar has been suggested by a number of authors (de Vaucouleurs, 1964; Blitz & Spergel 1991 and references therein), although often it was predicted to be inclined by $\sim 30^\circ$. If the bar is pointing near the line of sight, it can be considered to be an ‘efficient’ structure for generating microlensing because the mass in such a bar is concentrated along the line of sight toward the source stars. Paczyński *et al.* (1994) suggested that a bar with a small inclination angle might provide the large observed optical depth, and Zhao *et al.* (1995) have developed a detailed bar model. Toward Baade’s Window, they find an optical depth of $\tau = 1.7 \times 10^{-6}$ due to lensing by the bar and $\tau = 5 \times 10^{-7}$ due to lensing by a truncated disk.

We have seen in a previous section that this truncated disk seems to be in conflict with our observations of microlensing of stars on the upper main sequence, but Zhao, *et al.* also quote an optical depth of $\tau = 6 - 9 \times 10^{-7}$ for an untruncated disk. Comparing with our optical depth results, we find that the total τ of 2.2×10^{-6} for the truncated disk model is formally ruled out at the 93% confidence level while if we take the maximum, untruncated disk model the total is $\tau = 2.6 \times 10^{-6}$ which can be formally excluded only at 85% confidence.

A model with a fairly massive disk and a massive axially symmetric bulge has been proposed by Evans (1995). He assumes that a rather large fraction of the stars observed are actually in the disk, but because we are considering only the clump giant sources, we will use his numbers for lensing of bulge stars. Similarly, we will also ignore the contribution from lensing by halo objects since it is unlikely that the Galaxy has a very massive halo composed of substellar Machos (Alcock *et al.* 1995c, 1995d; Aubourg *et al.* 1995). Toward Baade’s window, the Evans model gives an optical depth of $\tau = 1.9 \times 10^{-6}$ with half the contribution from disk lensing and half from bulge lensing. This value is formally excluded at the 95% confidence level.

Finally, we should mention one caveat to the optical depth comparisons mentioned in this section. Most of the calculations of the optical depth due to lensing by the bulge or bar have assumed that we have a magnitude limited sample of stars so that we can see a larger fraction of the stars near the front of the bulge than toward the back. For the clump giant sample considered here, a better assumption would be that our source stars represent a complete set of stars that can be seen throughout the bulge. The adoption of this assumption would increase the predictions of some of the models mentioned above, but the main conclusion, that the most of the recently proposed models can marginally fit our optical depth measurement should remain unaffected by this correction.

However, if further data reveals that the true optical depth is in fact close to or higher than our central value, this would prove rather hard to account for with the models proposed

to date.

8. Microlensing Event Timescales

In addition to the microlensing optical depth, the distribution of microlensing event timescales can also be used to constrain models. However, unlike the optical depth, the timescale distribution depends on the mass function and the spacial and velocity distributions of the lensing population. The formula for the Einstein Ring diameter crossing time is

$$\hat{t} = \frac{2}{v_{\perp}} \sqrt{\frac{4GmLx(1-x)}{c^2}} , \quad (8.1)$$

as can be seen from eq. (2.1).

Figure 7 is a histogram of the \hat{t} distribution of the 41 events which pass the cuts used in the optical depth determination, while Figure 8 is the histogram for the same events with each event weighted by its \hat{t} value which is proportional to its contribution to the optical depth. Figures 7 and 8 indicate while most of the events have short timescales ($\lesssim 40$ days), about a third of the contribution to the optical depth comes from the long time scale events. This might be taken as an indication of microlensing by the disk since most bulge microlensing models do not tend to predict many long timescale events (Kiraga & Paczyński 1994; Evans 1995). However, models with massive bars might also predict a reasonable number of long timescale events if the pattern rotation speed of the bar is large or if they contain a significant population of massive objects such as neutron stars.

It is convenient to use the Kolmogorov-Smirnov test to compare the observed distribution of \hat{t} with model predictions, but the K-S test can also be used to compare the \hat{t} distributions for different subsets of the data. Figure 9 shows the cumulative distributions of event timescales for the clump giant events compared to the other bulge events. It is clear that the clump giant events have significantly longer time scales and the probability that this could have occurred by chance is $P_{KS} = 0.007$. The reason for this difference is not well understood at present, but there are several known factors that contribute to this. First, the spatial distribution of the clump giants and the ‘non-clump giants’ is different. The clump giants are concentrated more toward the Galactic Center at low Galactic latitudes. Thus, the clump giants are somewhat more likely to be lensed by disk stars than the ‘non-clump giants’ which would be preferentially lensed by other Bulge stars which would give them somewhat shorter timescales. However, the difference between the center points of each of these distributions is only about 0.3° in latitude, so this seems unlikely to account for all of the difference.

Another factor which may be somewhat more important is blending. The clump giants are unlikely to be blended significantly, but the ‘non-clump giants’ tend to be much fainter and some of them are probably seriously blended. The fit \hat{t} values for blended stars are often significantly underestimated. A final effect that might influence the \hat{t} distribution is the location of each set of stars along the line of sight. The clump giants are generally

located in the Bulge, but the ‘non-clump giants’ include a significant fraction of foreground disk stars. Thus, some of the ‘non-clump giant’ events may be due to disk-disk lensing. Unfortunately, this last effect has the wrong sign to explain the difference between the \hat{t} distributions because the disk-disk lensing events should have larger average \hat{t} values.

Figure 10 shows a comparison of the clump giant \hat{t} distribution to the Evans (1995) model discussed above. Evans assumes a Scalo (1986) mass function for the disk lenses and a Richer-Fahlman (1992) mass function for the bulge. The Richer-Fahlman mass function rises very steeply for low masses and this gives rise to a great many short timescale microlensing events. This model is clearly ruled out by the K-S test which gives $P_{KS} = 0.0009$. Of course, if we are free to choose our mass functions, we could replace the assumed Richer-Fahlman mass function for the bulge component of Evans model with something which fits our observations, and so a test such as this cannot rule out bulge models unless we are willing to assert that the implied mass function is unreasonable on other grounds. The determination of the mass model by comparison to the OGLE microlensing observations is the approach taken by Zhao *et al.*(1995), so a similar test is not possible with their model.

8.1. TIMESCALES FOR A BAR MODEL

We have also estimated timescale distributions for the Han & Gould (1995a) bulge model, for various mass functions. We use a barred bulge as in Han & Gould, with a density profile

$$\rho_B = 2.07 \exp(-w^2/2) \text{ M}_\odot \text{ pc}^{-3},$$

$$w^4 = \left[\left(\frac{x'}{1580 \text{ pc}} \right)^2 + \left(\frac{y'}{620 \text{ pc}} \right)^2 \right]^2 + \left(\frac{z}{430 \text{ pc}} \right)^4 \quad (8.2)$$

Here x', y' are measured along the axes of the bar in the galactic plane; the x' axis is aligned 20° from the GC-Sun line, with the near side of the bar in the positive- l quadrant, and z is the usual height above the galactic plane. The total bar mass in this model is $20.65 \rho_0 abc$, where a, b, c are the scale lengths above; i.e. $M = 1.8 \times 10^{10} \text{ M}_\odot$ for our chosen values.

We use a double-exponential disk with a density profile

$$\rho_D = 0.08 \exp((R_0 - s)/3.5 \text{ kpc}) \exp(-|z|/325 \text{ pc}) \text{ M}_\odot \text{ pc}^{-3}, \quad (8.3)$$

where s, z are Galactocentric coordinates in cylindrical polar coordinates.

These models give optical depths towards Baade’s Window of 1.3×10^{-6} from the bar, and 0.6×10^{-6} from the disk.

We assume that the velocity distribution function for the bar is a Gaussian with a dispersion of 110 km/s in each transverse direction, and for the disk is a flat rotation curve of 220 km/s with a Gaussian dispersion of 30 km/s in each direction. We assume that sources reside in the bar, and are distributed in distance proportional to the local density (i.e. the luminosity function cancels the change in volume element, or $\beta = -1$ in the notation of Kiraga & Paczynski (1994)).

Using a Monte-Carlo simulation with the above parameters, we have evaluated the distribution of event timescales \hat{t} for several illustrative mass functions: delta-functions at 0.1 and $1 M_\odot$, a Scalo (1986) main-sequence PDMF, and two power-law mass functions with $\phi(m) \propto m^{-\alpha}$: one with $\alpha = -2.3$ for $0.1 < m < 1.4 M_\odot$, and one with a large number of brown dwarfs, with $\alpha = -2$ for $0.01 < m < 1.4 M_\odot$. A broader class of models has been studied by Han & Gould (1995c), with fairly similar conclusions to those below.

Results are shown in Figure 11 for our sample of 41 bona fide microlensing candidates which pass the cuts (excluding the 2 probable variables). We include the detection efficiency $\mathcal{E}(\hat{t})$ in the model predictions, and normalize the model predictions to the observed number of events. Given the systematic uncertainties both due to crowding and the fact that the bulge velocity structure is not well known, it is unwise to quote rigorous significance levels, but several general conclusions can be drawn.

- (i) Note that the range of model timescales is large even for the delta-function mass functions. This means that it will be very hard to extract information about fine details of the mass function. However, the mean mass of the lenses can be fairly well constrained, and microlensing has the major advantage that the estimate is independent of the luminosities of the lenses.
- (ii) The observed range of timescales is roughly consistent with most of the lenses being low-mass stars in the range $0.1 < m < 1 M_\odot$. There is some evidence for an excess of short-timescale events over the predictions from the Scalo (1986) PDMF; as noted by Han & Gould (1995c), a power-law with $\alpha = -2.3$ provides a better fit. However, this could also possibly be explained by blending causing the fitted event timescales to be systematically shortened.
- (iii) The mass function with a large mass fraction ($\approx 45\%$) of brown dwarfs predicts many more short-timescale events ($\hat{t} < 10$ days) than observed; thus, the disk and bulge mass are probably dominated by objects more massive than $0.1 M_\odot$, though a modest fraction of brown dwarfs would be allowed.
- (iv) There is marginal evidence for an excess of long-timescale events ($\hat{t} > 100$ days) relative to the Scalo and power-law PDMF's. This could be due to an additional population of massive lenses; ordinary stars with $m \gtrsim 1.5 M_\odot$ would be brighter than our typical source stars so are excluded, but a substantial population of neutron stars or black holes is possible. The statistical significance of this excess is not large, and it could also be explained by a population of slower-moving objects with a conventional mass function. Although more statistics are clearly desirable, these 4 long events are interesting because they contribute about a third of the estimated optical depth.

9. Implications of Microlensed Main Sequence Stars

Although Figure 4 indicates that the brighter main sequence stars are less likely to be microlensed than giants of similar brightness, the fact that *any* microlensing events are seen along the bright main sequence is actually difficult to explain in some Galactic models. Based on an analysis of the OGLE color magnitude diagrams, Paczyński *et al.* (1994) have argued that the Milky Way disk has a hole in the center starting 3-4 kpc from the solar radius. They also argue that the stellar density through the disk stays nearly constant along the line of sight to Baade's Window because the effect of the rising exponential scale length tends to cancel the effect of the falling exponential scale height. This would be a reasonable approximation for our data as well because our average galactic latitude is close to that of Baade's Window. With this assumption, it is straightforward to show that the optical depth to disk lensing is 4 times larger for stars in the Galactic bulge than for those in the disk.

Of course, bulge stars may be lensed by other bulge stars, as well. Since a truncated disk has a small microlensing optical depth, a Galactic bar pointed along the line of sight is probably required to explain the microlensing results in these models. In the bar model of Zhao, Spergel & Rich (1994), which assumes a truncated disk, the disk only accounts for 20% of the total optical depth. This implies that the predicted optical depth toward the disk main sequence stars should be only 5% of the optical depth toward the giants because the disk stars can only be lensed by other disk stars and because the average distance to the disk stars is about 1/4 of the distance to the giants in the Bulge. Now for disk-disk lensing, the source, lens, and observer are all rotating at nearly the same velocity, so the value of v_{\perp} should be very small, and the \hat{t} values should be larger than for lensing of bulge sources. This would imply the event rate for main sequence stars should be *smaller* than 5% of the rate for the giants. As we discuss below, we find 13 events in the 1.3 million stars which fall into our clump giant category. If we select all the stars which fall to the left of the clump giant region which are brighter than $V_M = 17.5$, then we have 500,000 stars in this bright main sequence region. At 5% of the observed rate toward the giants, we would expect to find 0.25 events in this category. Figure 4 shows 3 events in this category, but one of these events is 111-B which fails our final cuts because its t_{\max} is too late. The Poisson probability of finding 2 or more events when 0.25 are expected is only 2.6%, so the model of Zhao, *et al.*, combined with the OGLE truncated disk model would appear to be formally excluded.

More specifically, this analysis indicates that at least one of the following should be true:

- 1) The bright ‘main sequence’ seen towards the Bulge contains a significant number of stars further away than 4 kpc. These could be true main sequence stars or perhaps blue horizontal branch stars.
- 2) Disk lenses contribute significantly more than 20% of the microlensing optical depth toward the Bulge.

10. Implications for the Dark Matter Halo

The large microlensing optical depth seen toward the Galactic bulge was not predicted by “standard” Galactic models (Griest *et al.* 1991; Paczynski 1991). The models that have been proposed to explain these microlensing results tend to require that the mass of Galactic disk plus the bulge (or bar) is higher than has previously been supposed (Kiraga and Paczynski 1994; Evans, 1995; Zhao, Spergel and Rich 1995; Han and Gould 1995a,b,c; Gates, Gyuk, and Turner 1995a,b,c). If the mass of the disk plus bulge in the inner Galaxy is larger than previously thought, then for a given acceleration at the Solar circle, one would expect that the mass of the halo (the only remaining component) would be smaller in the inner regions of the Galaxy than previously thought. This in turn would lead one to infer a higher Macho *fraction* in the halo, for a given estimate of the microlensing rate toward the LMC. Thus, while the microlensing surveys toward the LMC can accurately constrain the mass of Machos along the line of sight toward the LMC (Alcock *et al.* 1995c, 1995d; Aubourg *et al.* 1995) they cannot determine the Macho *fraction* of the halo very accurately because the mass distribution of the Galactic halo is not well known.

In a previous paper, we considered our LMC results in some detail and gave examples of halo models which are consistent with a heavy disk (Alcock *et al.* 1995d). We showed that the most likely Macho fraction of the halo can increase by as much as $\sim 40\%$ when a ‘standard’ halo model is replaced by a heavy disk galactic model with a flat rotation curve. It may even be possible to construct models which are consistent with a 100% Macho halo and with galactic mass estimates based on satellite galaxies (e.g. Zaritsky *et al.* 1989) if the disk is heavy. Thus, it will be important to understand the source of the large microlensing optical depth seen toward the Galactic bulge before the microlensing optical depth toward the LMC can be accurately translated into a measure of the Macho fraction of the Galactic halo.

Gates, Gyuk, & Turner (1995a,b,c) have also considered the implications of the bulge lensing results on the MACHO fraction of the halo. They explored a large parameter space of models which comprised various combinations of halo, disk, and bulge. Gates *et al.* differ from us by concluding that a *higher* microlensing optical depth toward the Galactic bulge implies a *smaller* MACHO halo fraction. This conclusion arises as follows: the *disk* model in the Gates *et al.* simulations has a double exponential density profile, with a limit on the local column density. The local column density limit means that any model which has a massive disk will have a small radial scale length. When Gates *et al.* add a massive bar to a massive disk with a short scale length, they find that this puts too much mass near the Galactic center, which in turn produces a rotation curve inconsistent with observation in the inner Galaxy. Thus, they find that a massive bar *and* a massive disk are incompatible.

The conclusion of Gates *et al.* depends upon the assumption of a exponential disk. The actual disk density may differ substantially from the assumed exponential radial dependence. The implications of the microlensing results toward the bulge for the MACHO fraction of the halo remain unclear. More information from microlensing, including latitude and longitude dependence of the microlensing optical depth, will be needed to resolve this issue.

11. Future Developments

As mentioned above, we are continuing our microlensing survey of the Magellanic Clouds and the Galactic Bulge with significantly expanded galactic latitude and longitude coverage. This will aid us in determining the relative contribution to the microlensing optical depth from lenses in the Disk and Bulge or Bar.

Near the end of the the 1994 Bulge observing season, we developed the capability to detect events in progress (Alcock *et al.* 1994, Bennett *et al.* 1995, Pratt *et al.* 1995). This capability, which has also been demonstrated by the OGLE collaboration (Udalski *et al.* 1994c) allows detailed and comprehensive studies of the microlensing events in progress. For example, our first real-time event led to the first spectral observations of a microlensing event in progress (Benetti *et al.* 1995); the spectrum was unchanged during the event, a strong confirmation of the microlensing hypothesis. We have discovered about 40 microlensing events in progress in the 1995 observing season (see <http://darkstar.astro.washington.edu/> for details). To take advantage of our real time detection capability, we now operate the CTIO 0.9m telescope for 13% of every night to obtain more accurate photometry of ongoing events. This gives us a higher sensitivity to detect ‘second order’ microlensing effects (such as parallaxes and caustic crossings) that will yield additional information about the masses and distances of the lenses. It also gives us an opportunity to confirm microlensing events which have poor light curve coverage in the Stromlo data.

The high microlensing rate seen toward the Galactic Bulge coupled with the ability to detect microlensing events in real time has caught the attention of the planetary sciences community (Tytler *et al.* 1995), for microlensing appears to be a very promising new approach for detecting planets around distant stars (Mao & Paczyński 1991, Gould & Loeb 1992). Briefly, if every lensing star has a Jupiter-like planet, then $\sim 15\%$ of microlensing events should show a deviation $\delta A/A > 5\%$ from the single-lens microlensing light-curve. Most such deviations would be quite short-lived (~ 1 day), so we could not reliably detect them in the present data; but there appears to be a fairly high probability that a serious microlensing follow-up effort will soon commence to search for the binary microlensing signature of a planet orbiting a lensing star.

12. Summary and Conclusions

We have presented the results of the first year MACHO Project microlensing survey towards the Galactic Bulge. In this dataset consisting of 12.6 million stars observed for 190 days, we have discovered 45 candidate microlensing events. These include many events with high amplifications and excellent signal-to-noise, and two events showing exotic second-order effects: one is the first observation of parallax in a microlensing event, and the other is a spectacular example of a binary lens (first seen by OGLE). The distribution of peak amplifications is consistent with the microlensing prediction, and the events are distributed all across the color magnitude diagram. The only reasonable interpretation of these data is that the large majority of these events are, in fact, microlensing.

An unexpected feature of the color magnitude distribution of events is the discovery of a couple of microlensed stars on the upper main sequence. This is quite surprising because these stars had been thought to be in the foreground of the vast majority of lenses. The existence of these events is difficult to reconcile with Galactic models (such as that of Zhao *et al.* (1995)) where $\lesssim 25\%$ of the microlensing optical depth is due to the disk unless a substantial fraction of the bright main sequence stars are more distant than 4 kpc.

For our determination of the microlensing optical depth toward the bulge, we have focused on a subset of 13 events in which the lensed stars are ‘clump giants’. These stars have the advantage that they are generally located in the Bulge with little contamination from foreground disk stars unlike the fainter stars in our sample. Another advantage of the clump giant sample is that they are bright enough so that the blending of stellar images does not have a significant effect on the microlensing detection efficiencies. With this sample of 13 events, we find a microlensing optical depth of $\tau_{CG} = 3.9_{-1.2}^{+1.8} \times 10^{-6}$. This is quite consistent with the OGLE result but marginally higher than the most recent theoretical predictions. Using our full sample of events, we find $\tau_{\text{all}} \approx 2.43_{-0.45}^{+0.54} \times 10^{-6}$ ($0.75/f_{\text{Blend}}(0.8/(1-f_{\text{Disk}}))$), where f_{Blend} gives the degradation of our detection efficiency due to stellar blending, and f_{Disk} is the fraction of our source stars in the foreground disk.

If the true optical depth is close to our central value, then the inner Galaxy probably contains more mass than in most Galactic models, and the dark halo may have a larger core radius than is usually supposed.

Acknowledgements

We would like to thank Wyn Evans for kindly providing the detailed timescale distributions for his galactic bulge and disk model. We are grateful for the support given our project by the technical staff at the Mt. Stromlo Observatory. Work performed at LLNL is supported by the DOE under contract W-7405-ENG. Work performed by the Center for Particle Astrophysics personnel is supported by the NSF through AST 9120005. The work at MSSSO is supported by the Australian Department of Industry, Science and Technology. K.G. acknowledges support from DoE OJI, Alfred P. Sloan, and Cotrell Scholar awards. C.S. acknowledges the generous support of the Packard and Sloan Foundations.

References

Alcock, C., Akerlof, C.W., Allsman, R.A., Axelrod, T.S., Bennett, D.P., Chan, S., Cook, K.H., Freeman, K.C., Griest, K., Marshall, S.L., Park, H.-S., Perlmutter, S., Peterson, B.A., Pratt, M.R., Quinn, P.J., Rodgers, A.W., Stubbs, C.W., & Sutherland, W., 1993, *Nature*, **365**, 621.

Alcock, C. *et al.*, 1994. *IAU Circulars* 6068, 6095.

Alcock, C. *et al.*, 1995a, *ApJ*, **445**, 133

Alcock, C. *et al.*, 1995b, *ApJ*, **449**, 28

Alcock, C. *et al.*, 1995c, *Phys. Rev. Lett.* **74**, 2867

Alcock, C. *et al.*, 1995d, *ApJ*, in press.

Alcock, C. *et al.*, 1995e, *ApJL*, **454**, L125.

Alcock, C. *et al.*, 1995f, in preparation

Aubourg, E., Bareyre, P., Brehin, S., Gros, M., Lachieze-Rey, M., Laurent, B., Lesquoy, E., Magneville, C., Milsztajn, A., Moscosco, L., Queinnec, F., Rich, J., Spiro, M., Vigroux, L., Zylberajch, S., Ansari, R., Cavalier, F., Moniez, M., Beaulieu, J.-P., Ferlet, R., Grison, Ph., Vidal-Madjar, A., Guibert, J., Moreau, O., Tajahmady, F., Maurice, E., Prevot, L., & Gry, C., 1993, *Nature*, **365**, 623.

Aubourg, E. *et al.*, 1995. *AAp*, **301**, 1

Bahcall, J.N., 1986. *Ann. Rev. Astron. Astrophys.*, **24**, 577.

Bahcall, J.N., Flynn, C., Gould, A., & Kirhakos, S. 1994, *ApJL*, **435**, L51

Bennett, D.P. *et al.*, 1995, AIP Conference Proceedings 336: *Dark Matter*, S. S. Holt, C. L. Bennett, eds., p. 77.

Bennett, D.P. *et al.*, 1996, in preparation

Benetti, S., Pasquini, L. & West, R., 1995, *AAp*, **294**, L37.

Blitz, L & Spergel, D.N. 1991, *ApJ*, **379**, 631

de Vaucoulers, G., 1964, IAU Symposium 20: The Galaxy and the Magellanic Clouds, eds., F.J.Kerr & A.W.Rodgers (Sydney: Australian Academy of Science), p. 195.

Evans, N.W., 1995, *ApJL*, 437, L31

Fux, R., & Martinet, L., 1994, *AAp*, **287**, L21

Gates, E.I., Gyuk, G. & Turner, M.S., 1995a, *ApJL*, **449**, L123

Gates, E.I., Gyuk, G. & Turner, M.S., 1995b, *Phys. Rev. Lett.* **74**, 3724.

Gates, E.I., Gyuk, G. & Turner, M.S., 1995c, preprint.

Gnedin, O.Y., Goodman, J., & Frei, Z. 1995, astro-ph/9501112

Gould, A., 1994, astro-ph/9408060

Gould, A., & Loeb, A., 1992, *ApJ*, **396**, 104

Gould, A., Miralda-Escude, J., & Bahcall, J.N., 1994. *ApJL*, **423**, L105.

Griest, K., *et al.* 1991, *ApJL*, **372**, L79.

Han, C. & Gould, A., 1995a, *ApJ*, **447**, 53

Han, C. & Gould, A., 1995b, *ApJ*, **449**, 521

Han, C. & Gould, A., 1995c, astro-ph/9504078

Kiraga, M & Paczyński, B. 1994, *ApJL*, **430**, L101

Kuijken, K. & Gilmore, G., 1989. *MNRAS*, **239**, 605.

Mao, S. & Paczyński, B., 1991. *ApJL*, **374**, L37

Marshall, S. *et al.*, 1994. In *Astronomy from Wide-Field Imaging*, Procs. IAU Symp. 161, eds. H. MacGillivray *et al.*, Kluwer.

Minniti, D., 1995. ESO Preprint 1103.

Paczyński, B., 1986, *ApJ*, **304**, 1.

Paczyński, B., 1991, *ApJL*, **371**, L63

Paczyński, B., Stanek, K., Udalski, A., Szymanski, M., Kaluzny, J., Kubiak, M., Mateo, M. & Krzeminski, W., 1994, *ApJL*, **435**, L113

Petrou, M., 1981. *Ph.D. thesis*, University of Cambridge.

Pratt, M. *et al.*, 1995. In *Astrophysical Applications of Gravitational Lensing*, Procs. IAU Symp. 173, eds. C. Kochanek & J. Hewitt, Kluwer.

Refsdal, S., 1964. *MNRAS*, **128**, 295

Richer, H.B. & Fahlman G.G., 1992. *Nature*, **358**, 383

Rix, H.-W. & Rieke, M.J., 1993, *ApJ*, **418**, 123

Rix, H.-W. & Zaritsky, D., 1995, *ApJ*, **447**, 82

Scalo, J.M., 1986, *Fund. Cosmic Phys.*, **11**, 1

Stanek, K.Z., Mateo, M., Udalski, A., Szymanski, M., Kaluzny, J. & Kubiak, M., 1994, *ApJL*, **429**, L73

Stubbs, C., Marshall, S.L., Cook, K.H., Hills, R., Noonan, J., Akerlof, C.W., Axelrod, T.S., Bennett, D.P., Dagley, K., Freeman, K.C., Griest, K., Park, H.-S., Perlmutter, S., Peterson, B.A., Quinn, P.J., Rodgers, A.W., Sosin, C., & Sutherland, W., 1993, *SPIE Proceedings*, **1900**, 192

Schechter, P.L., Mateo, M., & Saha, A., 1993, *PASP*, **105**, 1342

Tytler, D. *et al.*, 1995, in preparation.

Udalski, A., Szymanski, M., Kaluzny, J., Kubiak, M., Krzeminski, W., Mateo, M., Preston, G.W., & Paczyński, B., 1993, *Acta Astronomica*, **43**, 289

Udalski, A., Szymanski, M., Stanek, K., Kaluzny, J., Kubiak, M., Mateo, M., Krzeminski, W., Paczyński, B. & Venkat, R., 1994a, *Acta Astronomica*, **44**, 165

Udalski, A., Szymanski, M., Mao, S., Di Stefano, R., Kaluzny, J., Kubiak, M., Mateo, M. & Krzeminski, W., 1994b, *ApJL*, **435**, L113

Udalski, A., Szymanski, M., Kaluzny, J., Kubiak, M., Mateo, M., Krzeminski, W. & Paczyński, B., 1994c, *Acta Astronomica*, **44**, 227

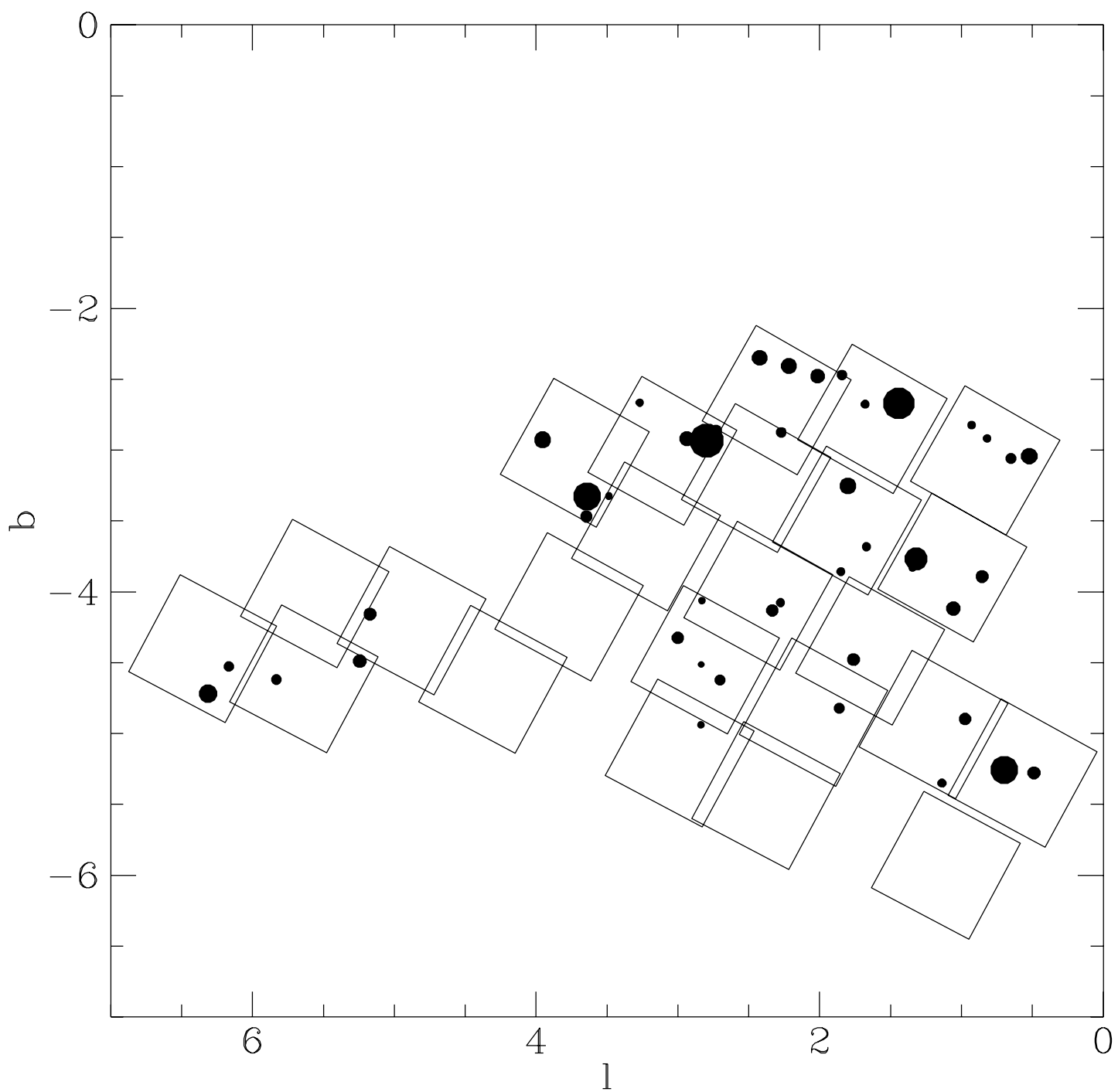
Weiland, J.L. *et al.*, 1994. *ApJL*, **425**, L81.

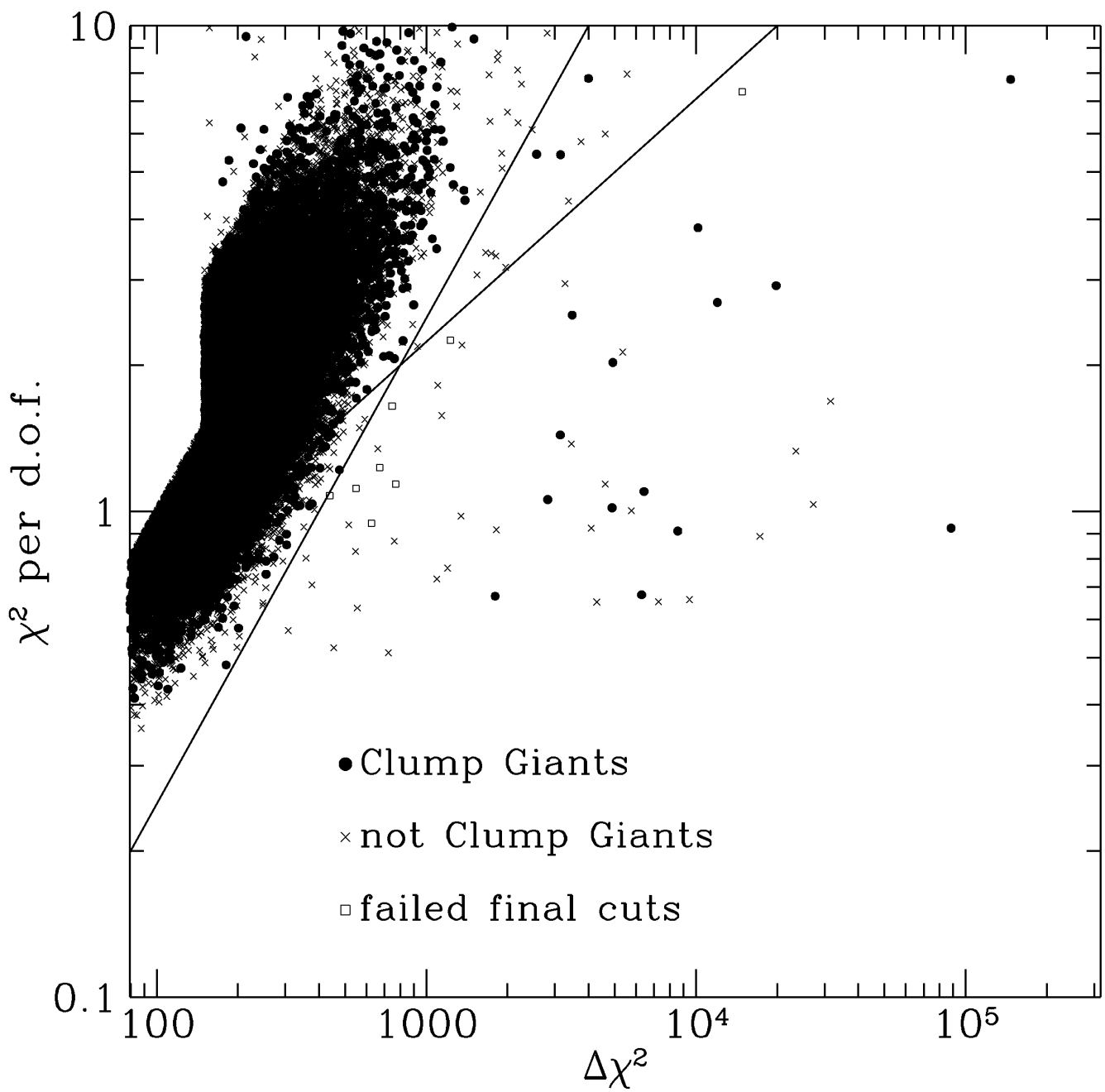
Zaritsky, D., Olszewski, E.W., Schommer, R.A., Peterson, R.C. & Aaronson, M., 1989. *ApJ*, **345**, 759.

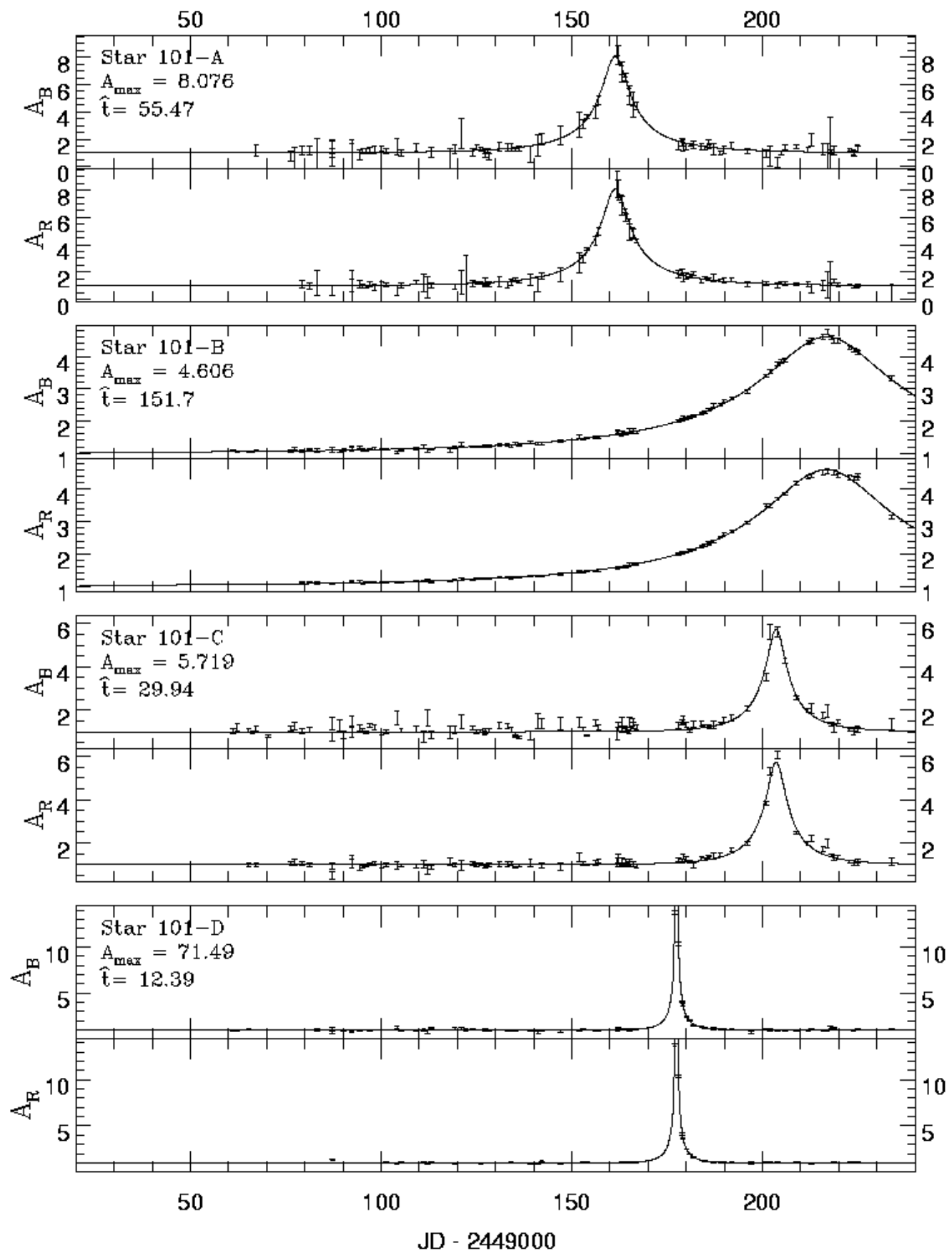
Zhao, H., Spergel, D.N., & Rich, M. 1995, *ApJL*, 440, L13

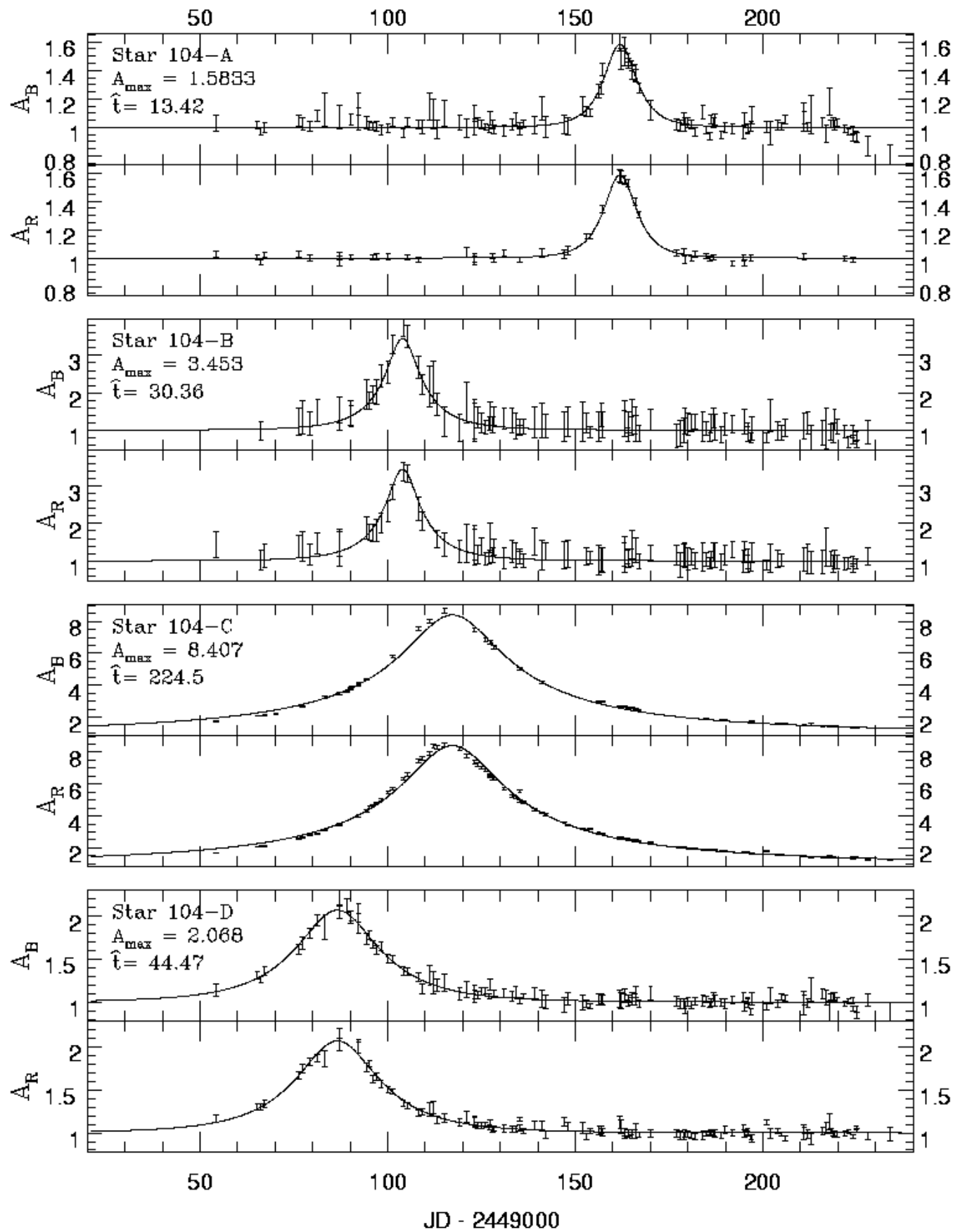
FIGURE CAPTIONS

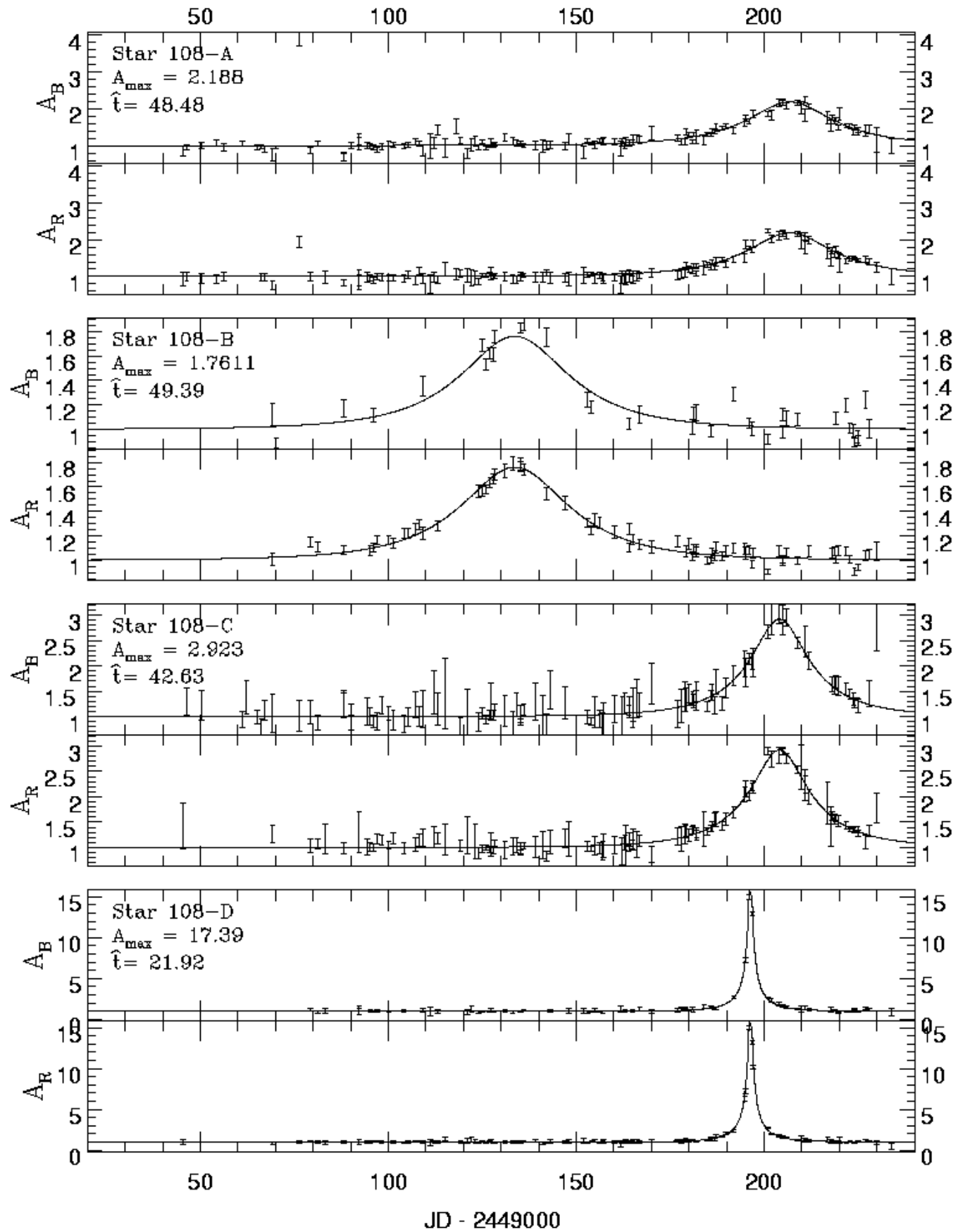
- 1) The locations of the 24 bulge fields presented in this paper are shown in Galactic coordinates. The dark spots indicate the locations of the events, and the area of each spot is proportional to the \hat{t} value for each event.
- 2) A scatter plot of the microlensing fit χ^2 (per d.o.f.) vs. $\Delta\chi^2$ which is the difference between the χ^2_{const} for a constant light curve fit and the microlensing fit χ^2_{ml} . The solid circles indicate stars classified as clump giants while the \times 's indicate stars outside the clump giant region of the color magnitude diagram. The squares indicate events which are removed by cuts on parameters not displayed in this figure.
- 3) Light curves for the MACHO blue and red pass bands are shown for the 45 events discussed in the text. The units are linear flux units normalized to the best fit unamplified flux given in Table 1.
- 4) The color magnitude diagram for each of the 45 event source stars along with a random selection of 7% of the stars in $5' \times 5'$ regions containing each of these stars. The unamplified locations of the lensed stars are indicated, and the ‘clump giant’ region defined in the text is shown as the region enclosed in the dashed contour.
- 5) The solid curve gives the sampling efficiencies for all stars while the dashed curve indicates the sampling efficiencies for the clump giant subsample. The clump giant sampling efficiency is a good approximation for the full efficiencies (including blending) for the clump giant sample.
- 6) The cumulative distributions of the impact parameter, u_{\min} , are compared to the predicted distributions for the full sample of events (a) and the clump giant subsample (b).
- 7) A histogram of the \hat{t} distribution of the 41 events used for the optical depth calculations.
- 8) A histogram of the \hat{t} distribution with each event weighted by its value of \hat{t} . This is roughly the same as weighting each event by its contribution to τ .
- 9) The cumulative \hat{t} distributions for the clump giant and non-clump-giant subsamples are plotted. The Kolmogorov-Smirnov (KS) test indicates that they are unlikely to have been drawn from the same distribution at the 0.7% confidence level.
- 10) The cumulative distribution for the clump giant subsample is compared to the theoretical prediction of the even Evans model. The KS test can be used to formally exclude the Evans model at 0.09% confidence.
- 11) Timescale distributions for 43/41 observed events (thick histogram) compared to predicted distributions, normalized to the observed number of events, for a fixed bar + disk density model (see text) with various mass functions. The two dashed lines show delta-functions at $0.1 M_{\odot}$ (left) and $1 M_{\odot}$ (right); the solid line is the Scalo PDMF; the long-dashed line is the power-law with $\alpha = -2.3$, $m_{lo} = 0.1 M_{\odot}$ of Han & Gould, and the dotted line is the ‘brown dwarf rich’ mass function with $\alpha = -2$, $m_{lo} = 0.01 M_{\odot}$.

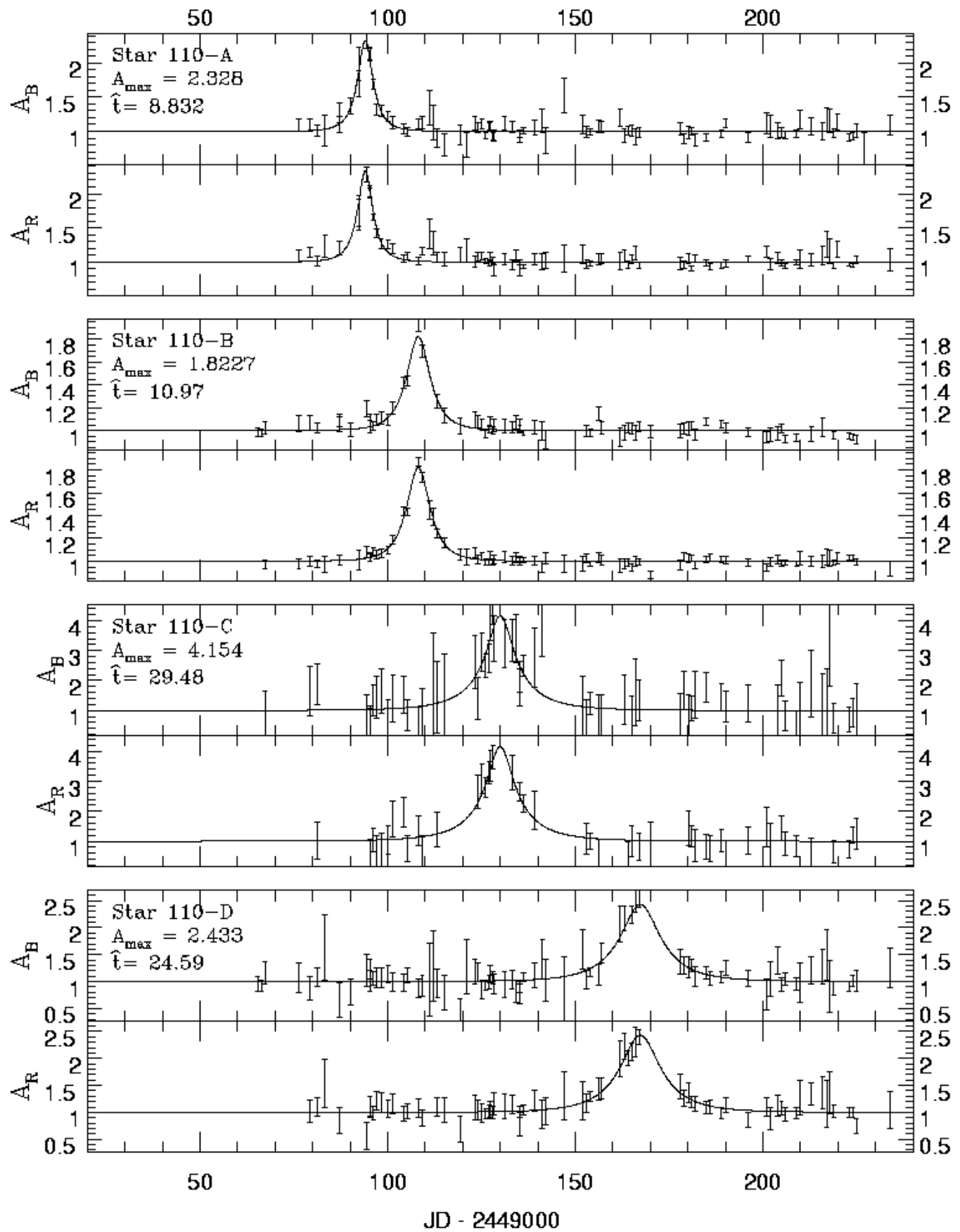


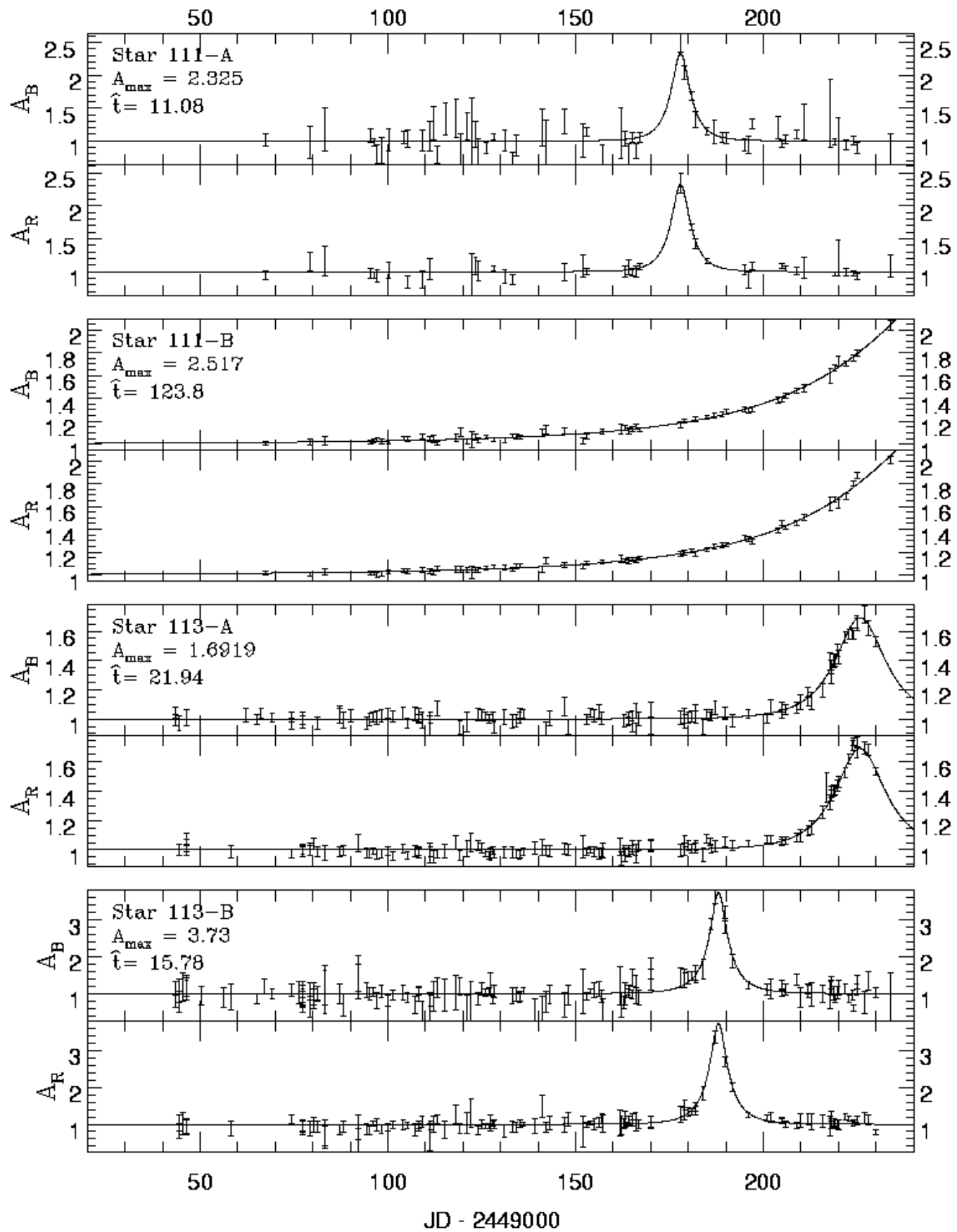


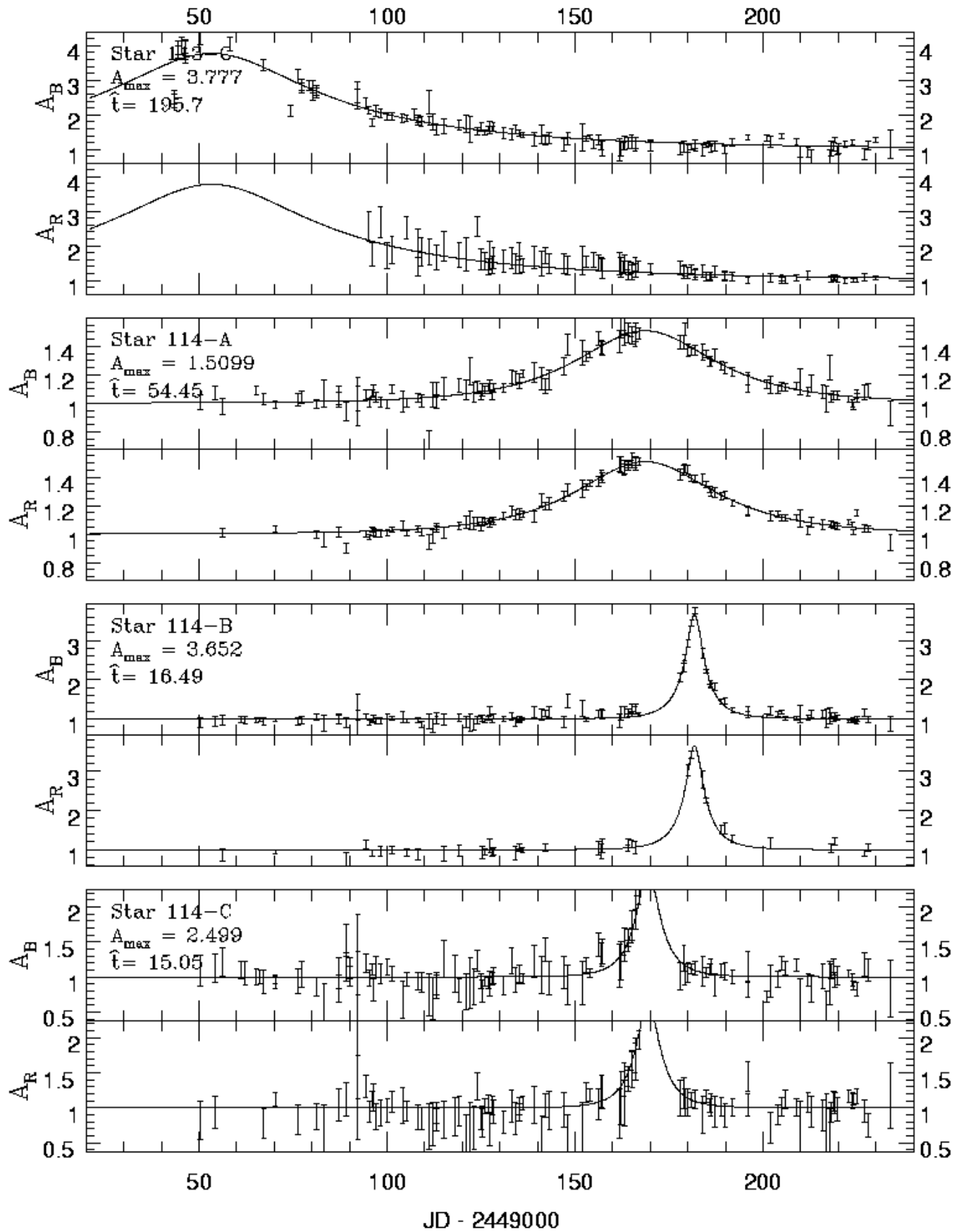


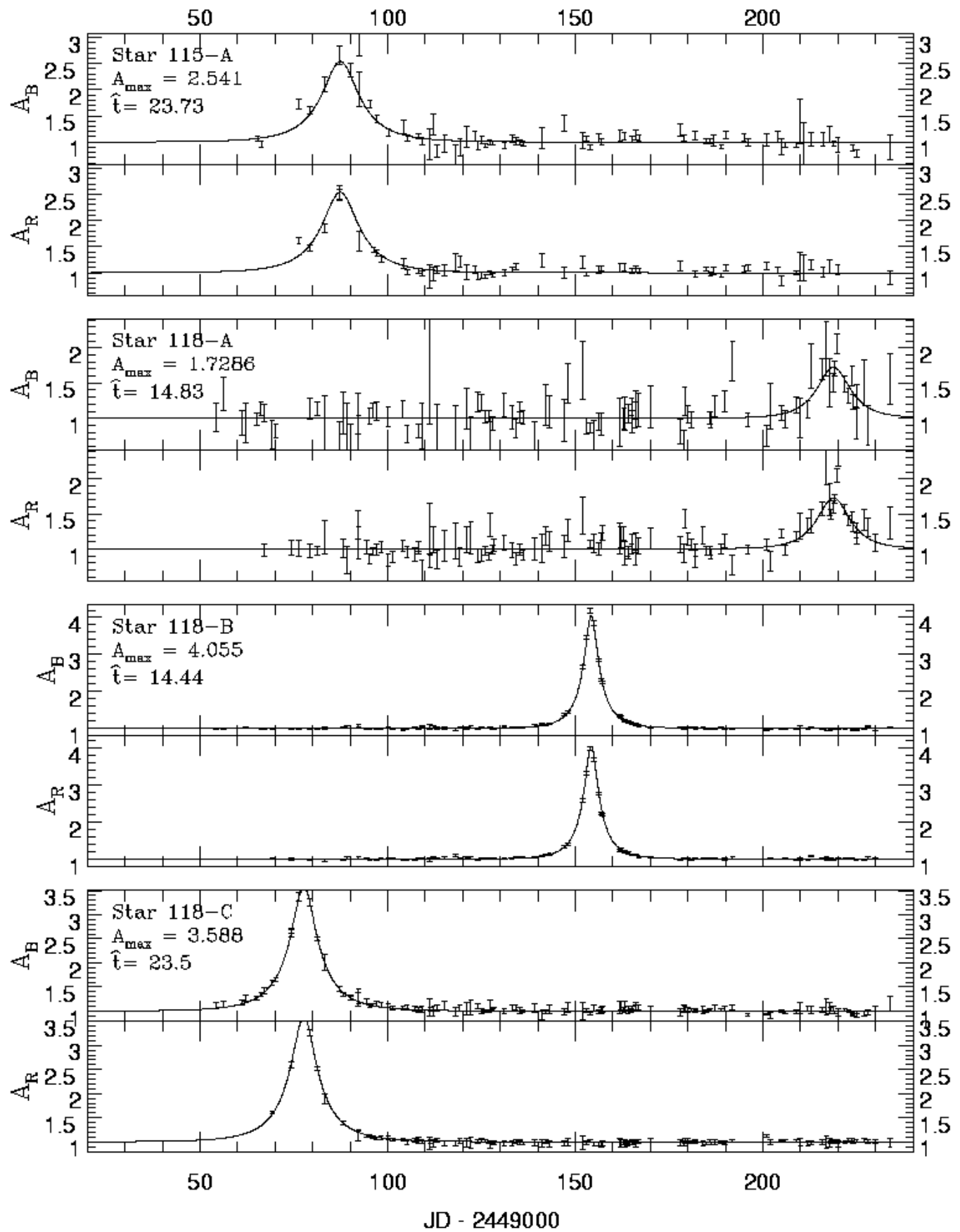


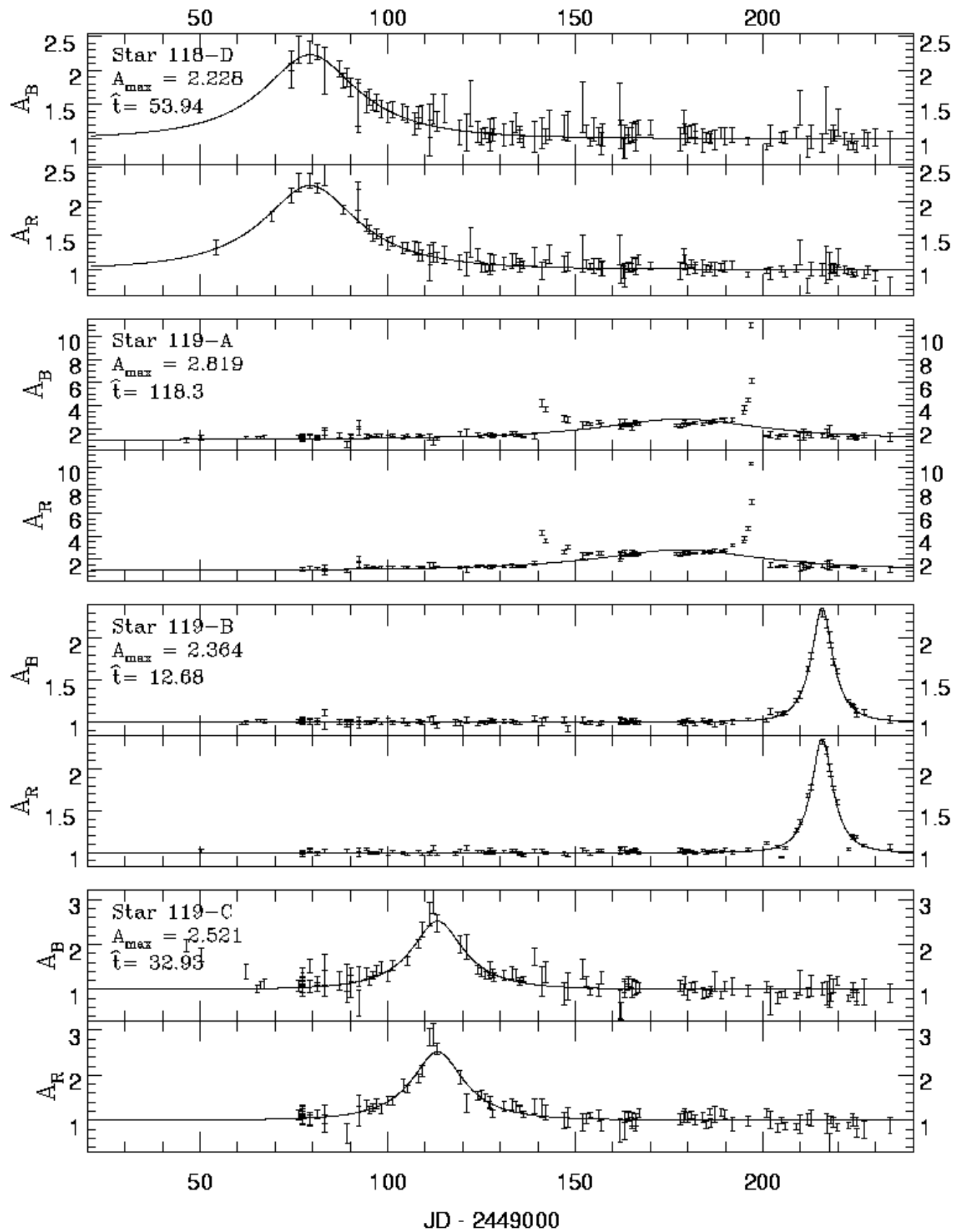


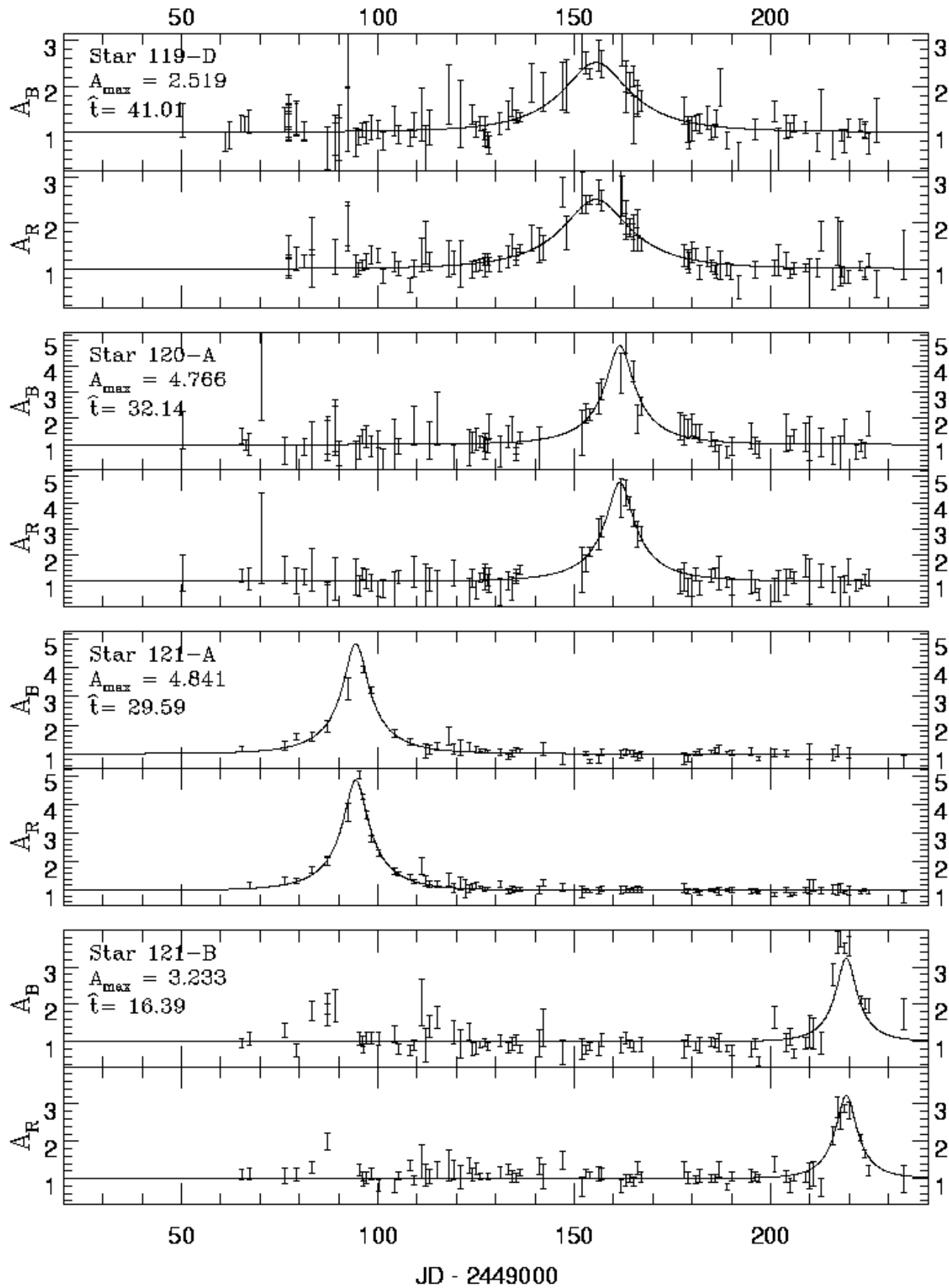


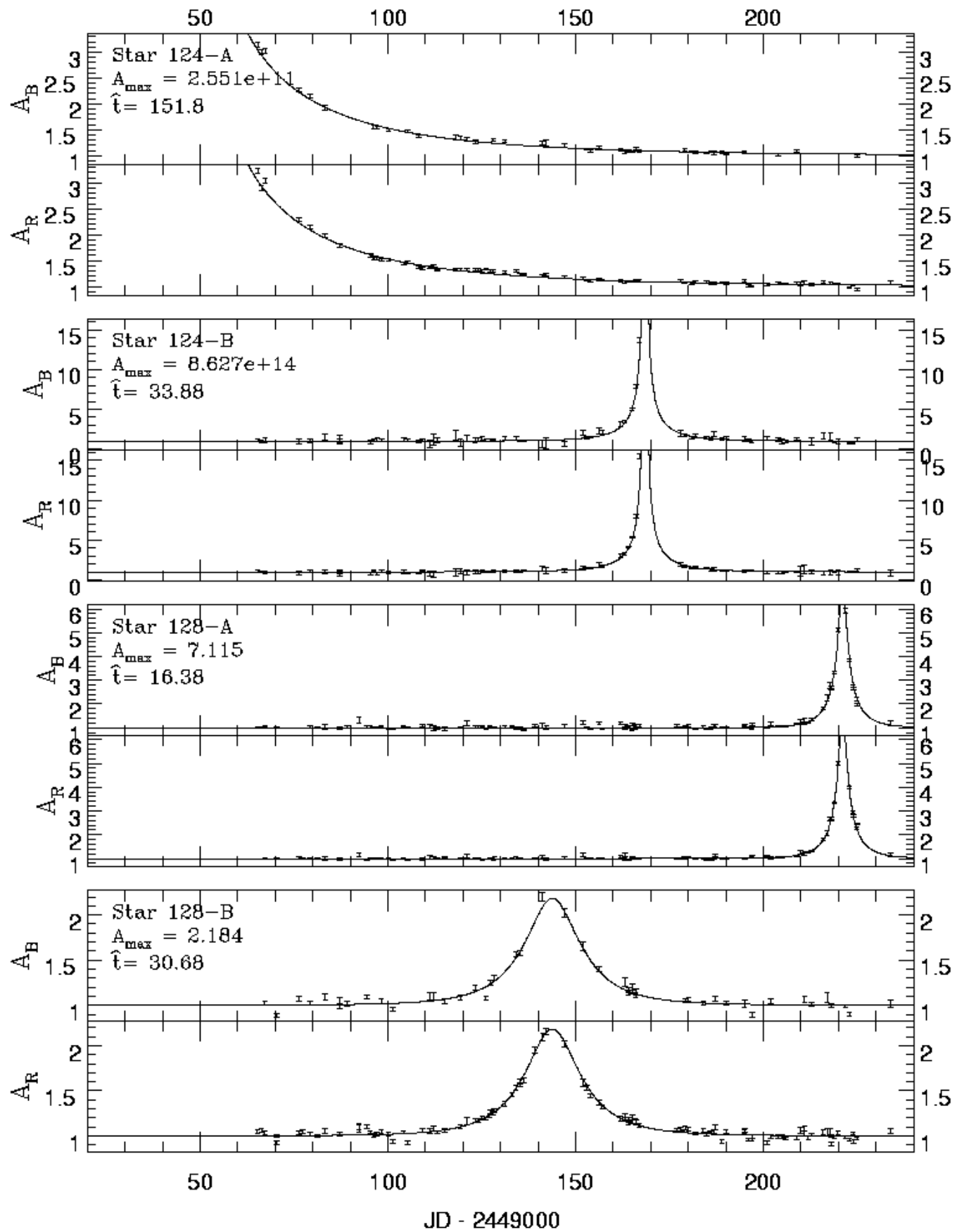


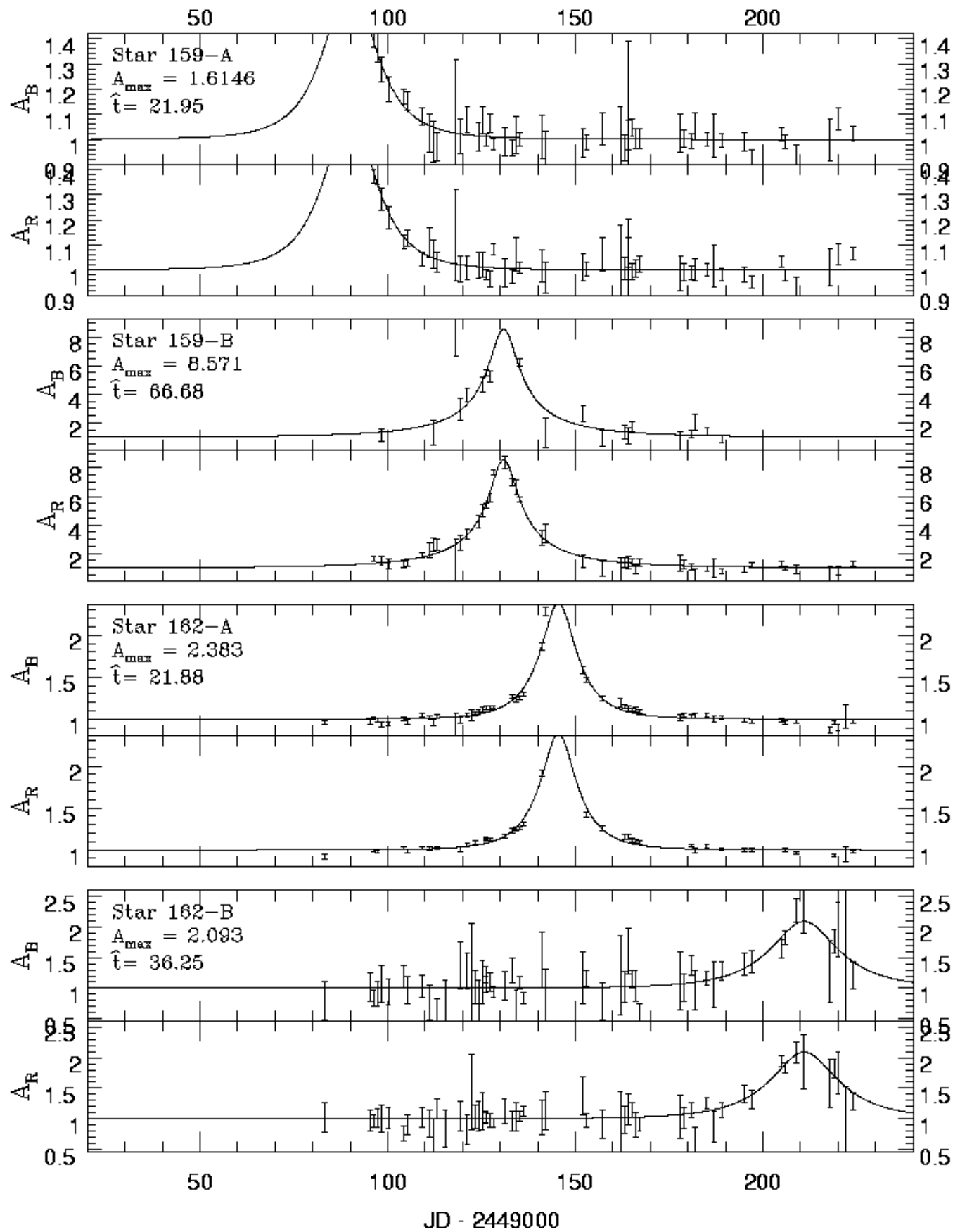


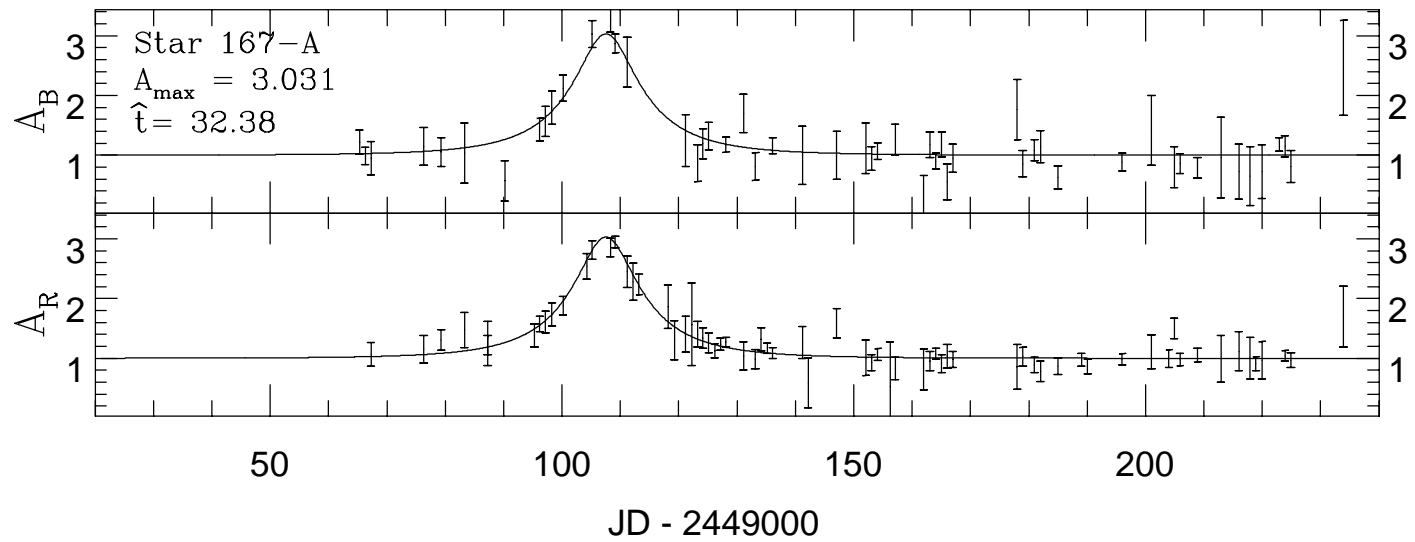


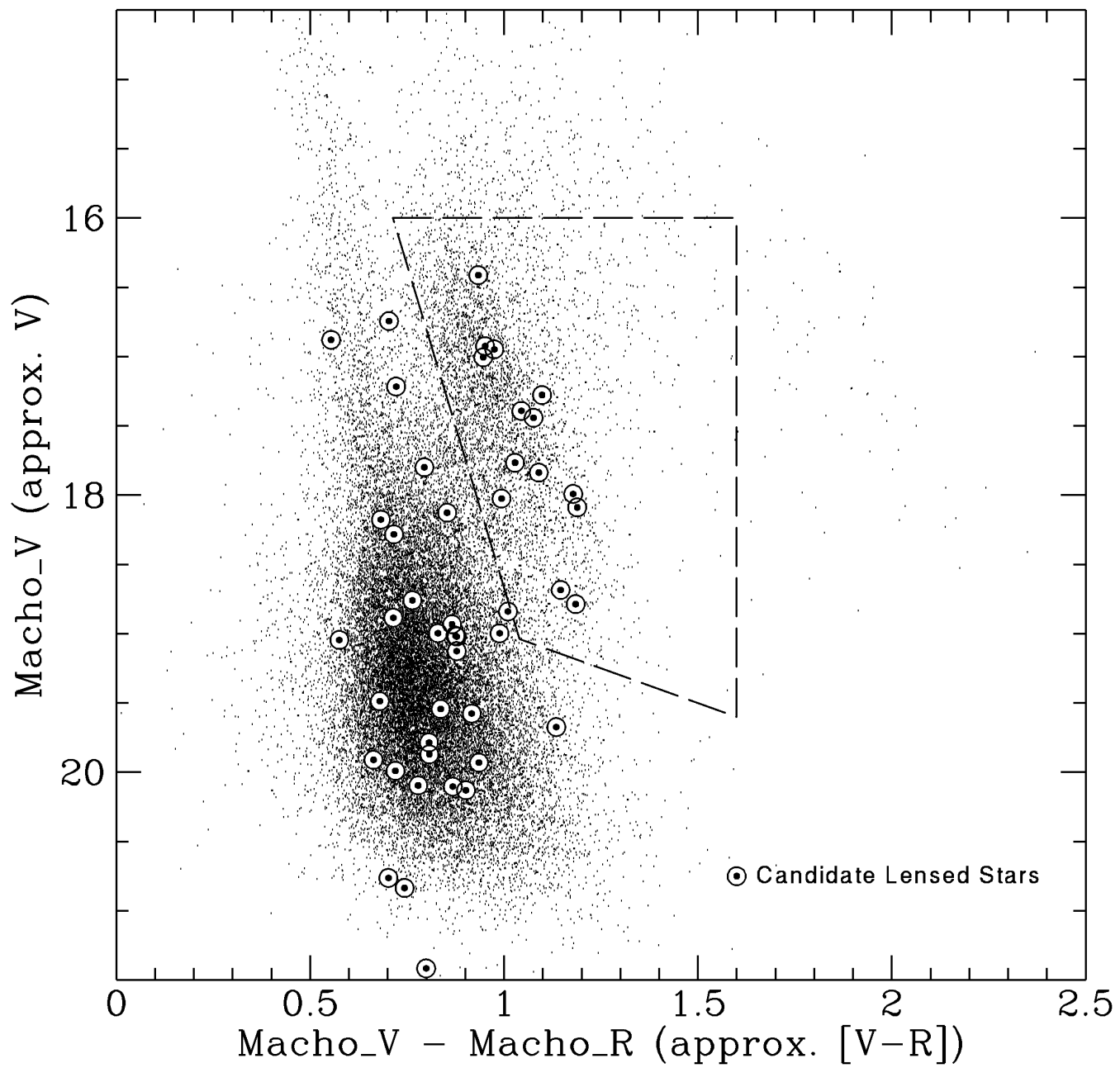


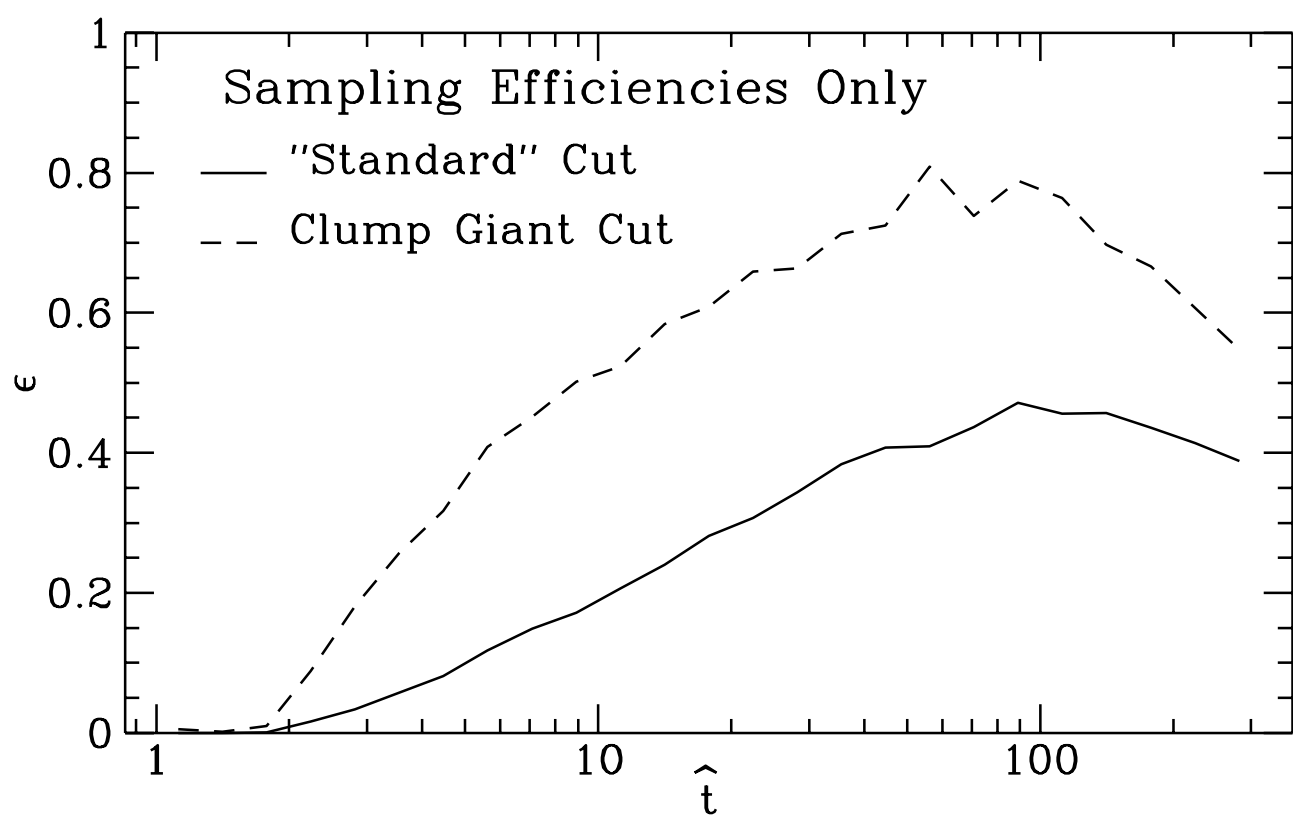


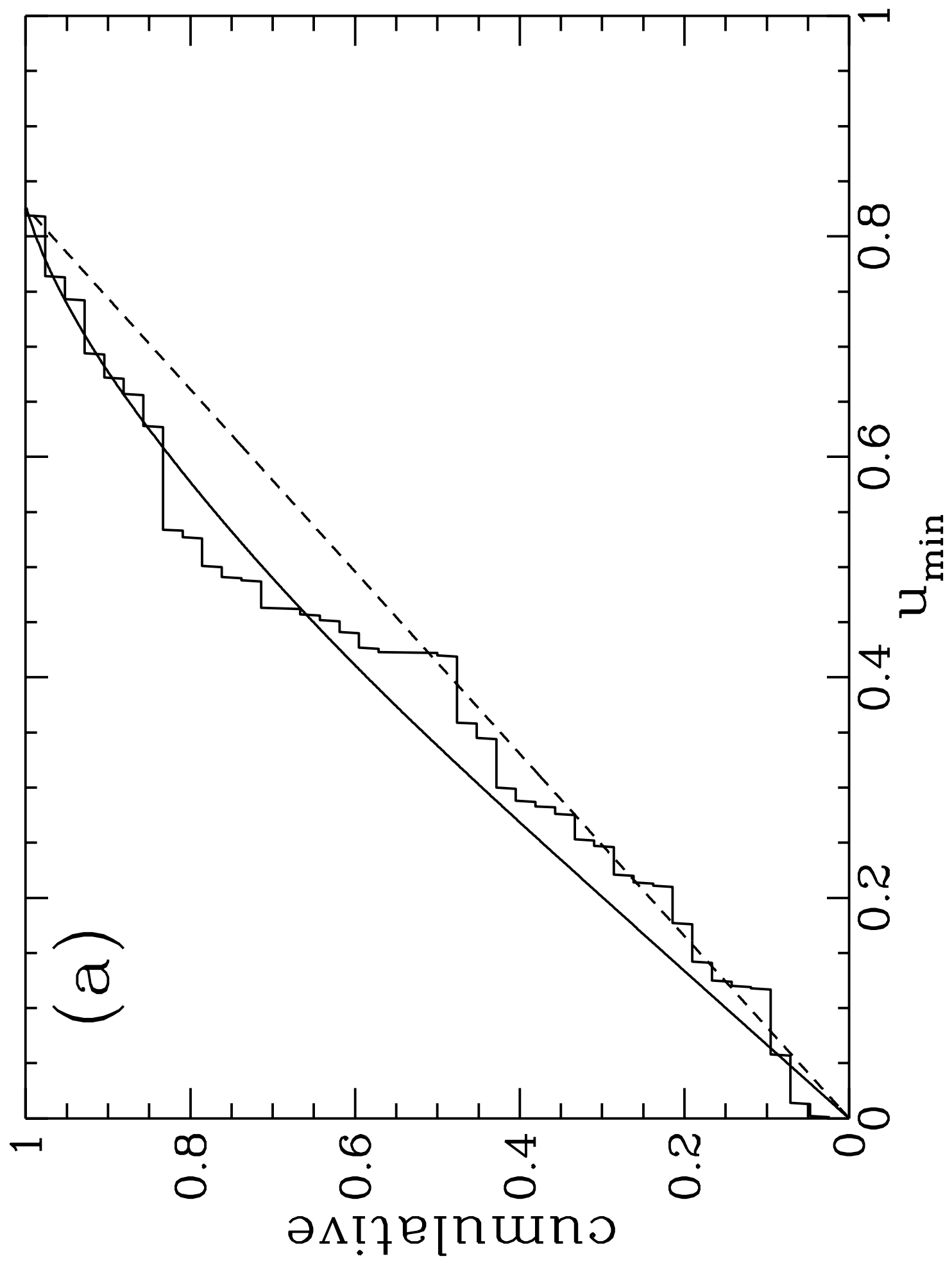


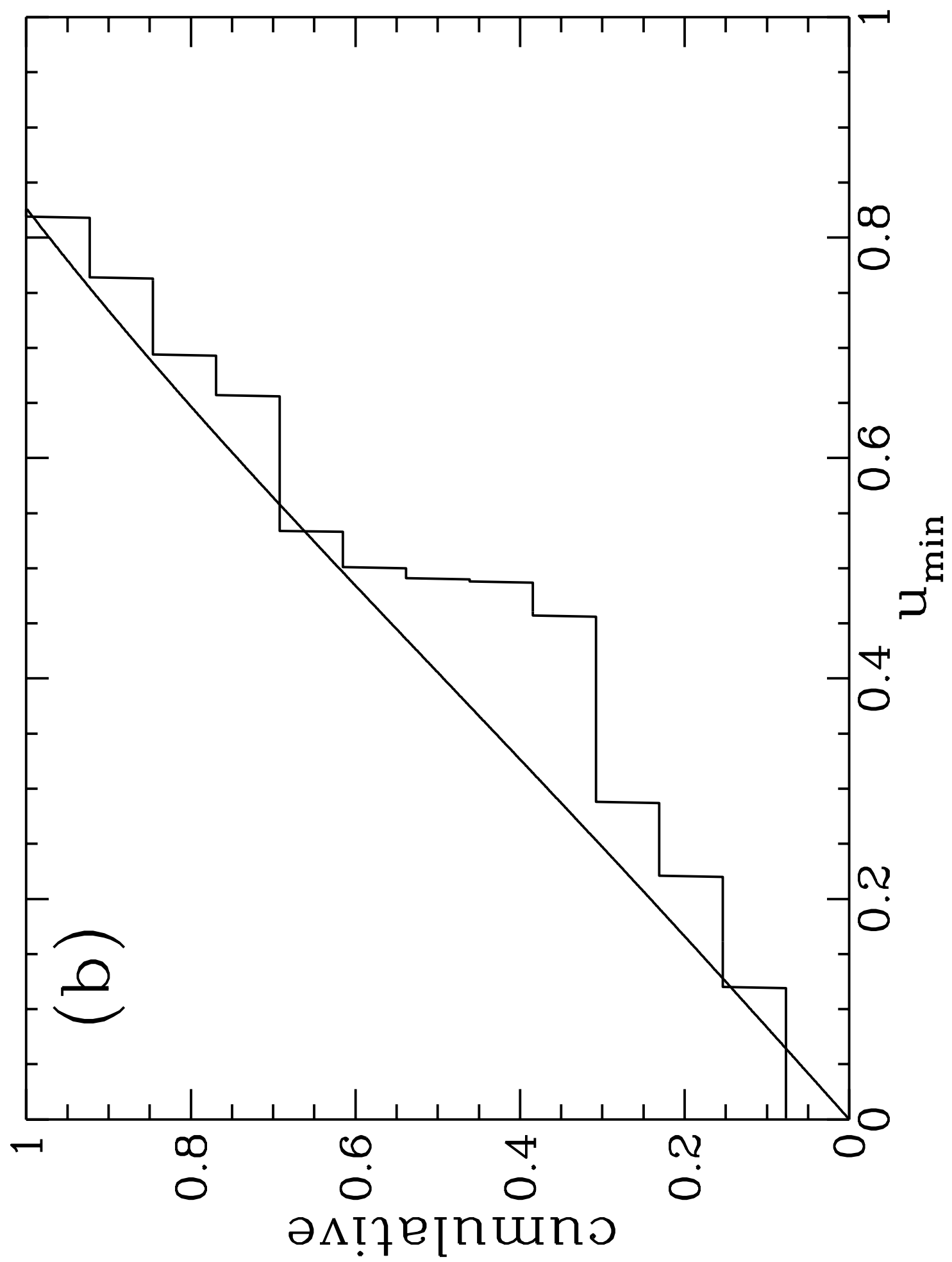


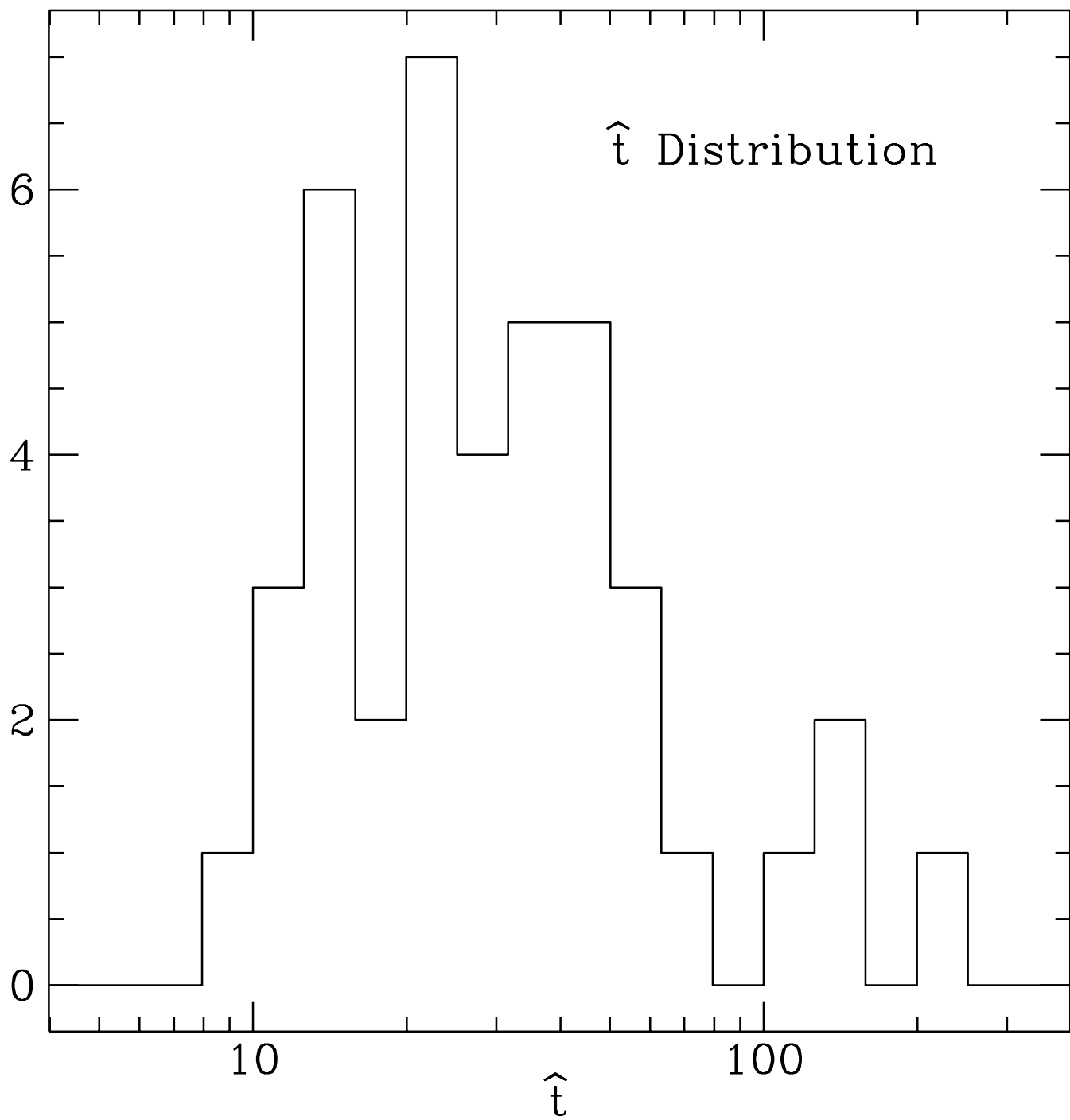


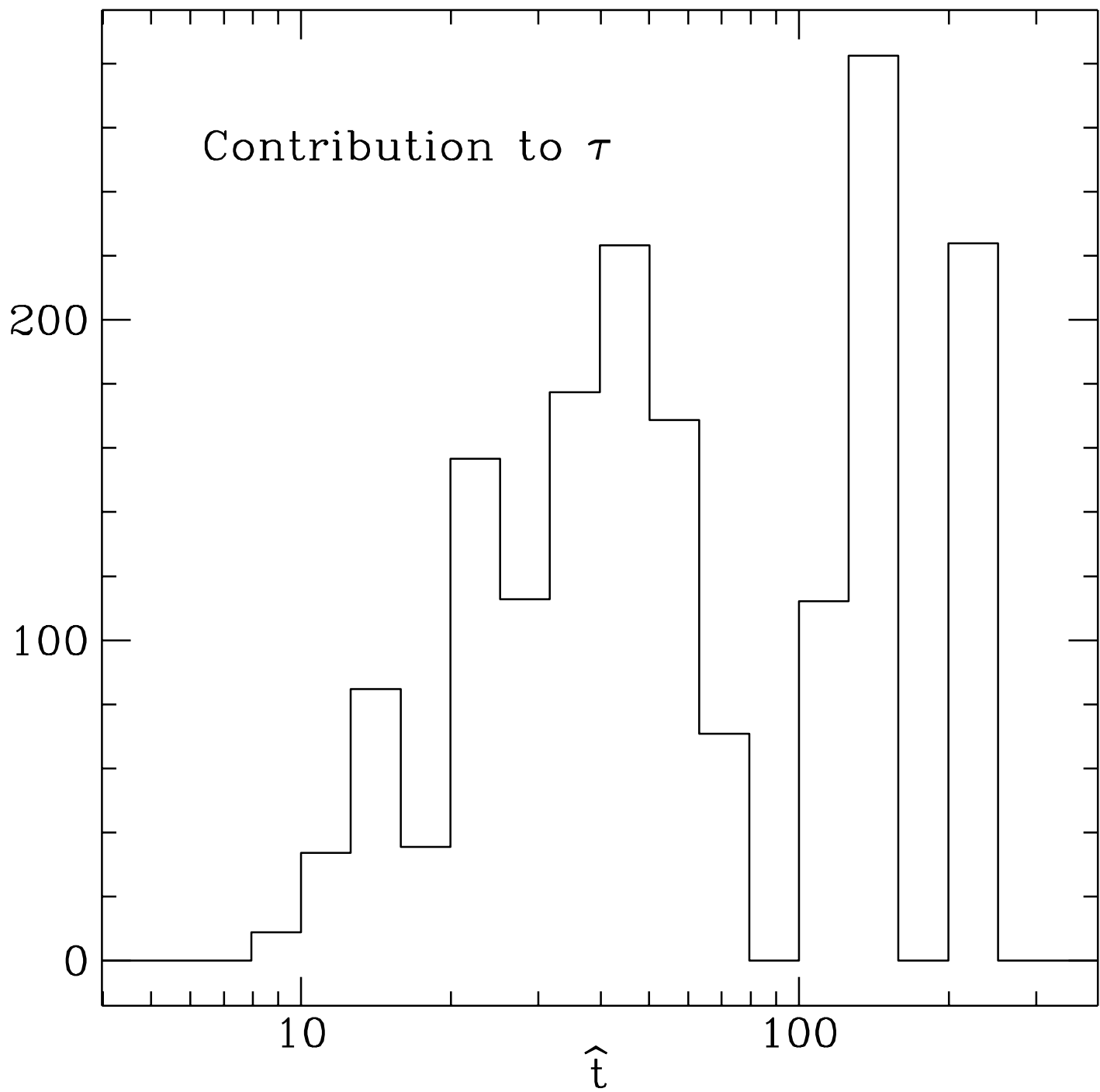


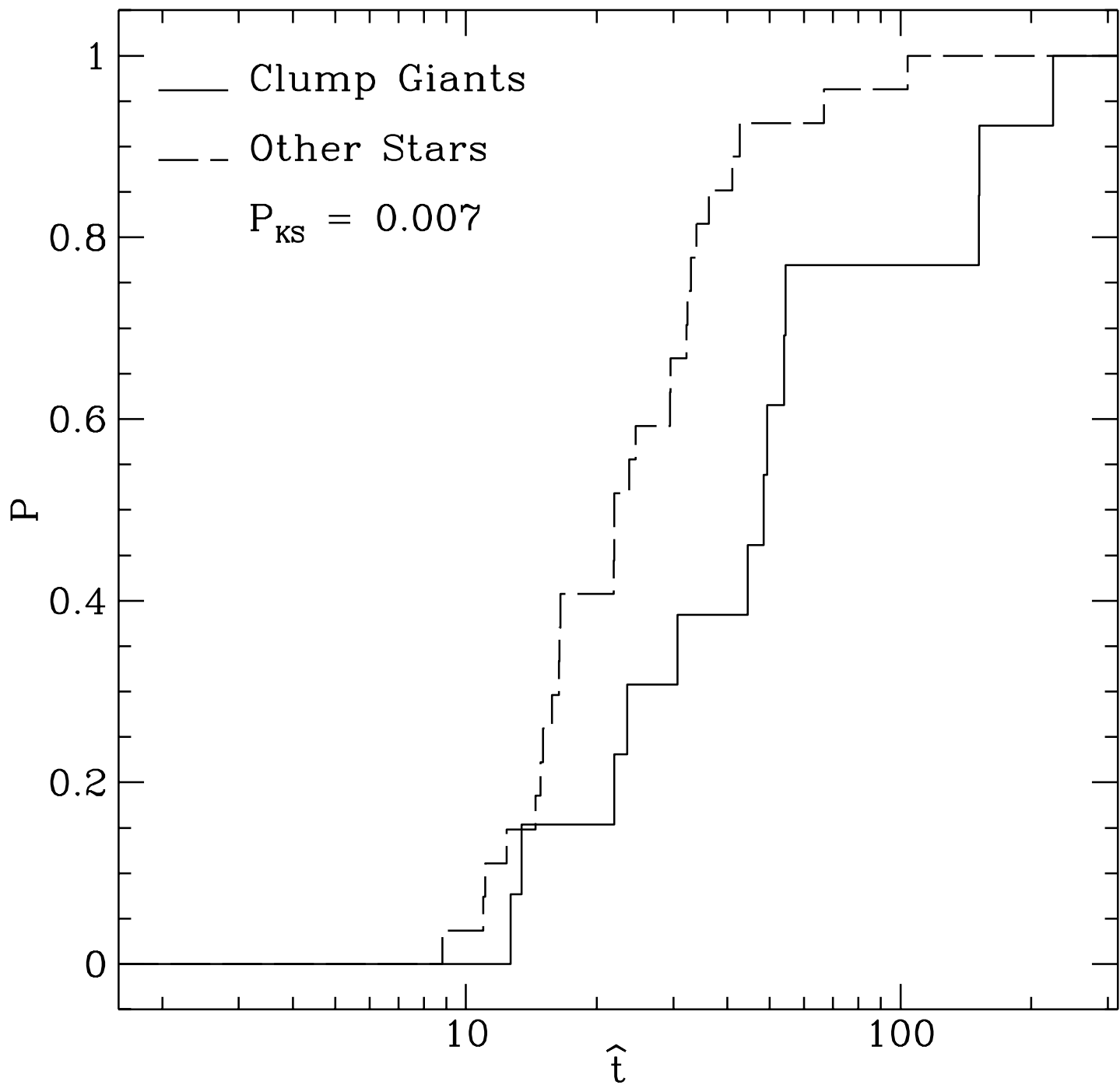












Event	RA (2000)	Dec (2000)	l	b	V	V-R	t_{max} (d)	\hat{t} (d)	A_{max}	χ^2
101-A	18 06 05.2	-26 59 38	3.95	-2.93	20.1	0.95	161.4±0.1	55.5±1.6	8.08±0.20	0.65
101-B ^c	18 06 58.3	-27 27 45	3.64	-3.33	17.3	1.1	216.8±0.1	151.7±1.0	4.61±0.02	0.952
101-C	18 07 32.6	-27 31 35	3.64	-3.47	19.5	0.8	203.6±0.1	29.9±0.5	5.72±0.10	2.13
101-D	18 06 37.6	-27 35 40	3.49	-3.32	18.8	0.8	177.400±0.004	12.4±0.1	71±31	1.33
104-A ^c	18 03 33.4	-27 27 47	3.27	-2.66	18.0	1.2	161.9±0.1	13.4±0.4	1.58±0.02	1.06
104-B ^f	18 03 09.0	-28 01 45	2.73	-2.86	19.0	1.0	104.0±0.3	30.4±1.8	3.45±0.11	0.51
104-C ^{c,p}	18 03 34.0	-28 00 18	2.80	-2.93	16.9	1.0	117.20±0.02	224.5±1.0	8.41±0.03	7.76
104-D ^c	18 03 29.0	-28 00 31	2.78	-2.92	18.0	1.0	86.6±0.2	44.5±0.9	2.07±0.02	1.10
108-A ^c	18 00 25.9	-28 02 35	2.42	-2.35	18.8	1.2	206.9±0.2	48.5±1.1	2.22±0.02	2.03
108-B ^c	18 00 11.5	-28 14 59	2.22	-2.41	17.8	1.1	133.7±0.4	49.4±1.6	1.76±0.01	2.54
108-C	18 00 01.3	-28 27 41	2.01	-2.48	19.7	1.1	204.1±0.2	42.6±1.1	2.92±0.04	0.65
108-D	18 02 09.9	-28 26 03	2.27	-2.87	19.0	0.95	196.31±0.01	21.9±0.4	17.4±0.3	0.89
110-A	18 09 56.0	-28 44 10	2.84	-4.51	19.1	0.95	94.0±0.1	8.8±0.5	2.33±0.07	0.958
110-B	18 08 07.3	-28 31 23	2.83	-4.06	17.8	0.8	108.1±0.1	11.0±0.4	1.82±0.02	0.952
110-C	18 09 32.5	-28 30 06	3.00	-4.32	21.4	0.8	130.0±0.3	29.5±3.5	4.15±0.38	0.57
110-D	18 10 04.9	-28 54 18	2.70	-4.62	19.8	0.8	167.3±0.5	24.6±1.8	2.43±0.09	0.53
111-A	18 11 39.2	-28 56 15	2.84	-4.94	18.9	0.95	177.9±0.4	11.1±1.2	2.33±0.12	0.954
111-B ^f	18 12 34.1	-29 09 15	2.74	-5.22	16.7	0.7	254.7±3.6	123.8±6.5	2.52±0.22	0.66
113-A ^c	17 59 35.9	-28 36 24	1.84	-2.47	17.4	1.0	225.8±0.2	21.9±0.7	1.69±0.01	0.67
113-B	18 00 02.9	-28 51 02	1.68	-2.68	19.6	0.95	188.0±0.1	15.8±0.6	3.73±0.14	0.77
113-C ^v	17 59 29.3	-29 03 11	1.44	-2.67	18.7	1.1	53.3±1.0	195.7±8.7	3.78±0.07	1.44
114-A ^c	18 02 36.8	-29 01 42	1.80	-3.25	17.8	1.0	168.6±0.2	54.4±1.4	1.51±0.01	1.02
114-B	18 04 02.2	-29 21 09	1.67	-3.68	18.3	0.7	181.7±0.1	16.5±0.4	3.65±0.06	1.00
114-C	18 05 08.6	-29 16 52	1.85	-3.86	19.0	0.6	169.4±0.5	15.0±1.2	2.50±0.3	0.80
115-A	18 09 02.9	-29 44 12	1.86	-4.82	18.9	0.7	87.3±0.2	23.7±0.8	2.54±0.07	1.82
118-A	17 58 55.6	-29 34 24	0.953	-2.82	19.9	0.9	218.8±0.3	14.8±1.1	1.73±0.03	1.35
118-B	17 59 03.3	-29 42 59	0.82	-2.92	16.9	0.6	154.20±0.02	14.4±0.1	4.06±0.03	1.03
118-C ^c	17 59 13.8	-29 55 53	0.65	-3.06	17.4	1.1	77.6±0.1	23.5±0.3	3.59±0.05	0.951
118-D ^c	17 58 52.5	-30 02 08	0.52	-3.04	18.1	1.2	79.3±0.6	53.9±2.3	2.23±0.04	0.67
119-A ^{b,o}	18 03 35.8	-29 42 01	1.32	-3.77	19.0	0.95	174.1±0.2	103.8±2.7	2.69±0.03	10.01
119-B ^c	18 03 54.1	-29 42 30	1.34	-3.83	16.9	1.0	215.75±0.04	12.7±0.1	2.36±0.02	2.69
119-C	18 03 03.0	-30 09 56	0.85	-3.89	19.5	0.7	113.3±0.3	32.9±1.1	2.52±0.07	1.58
119-D ^o	18 04 24.8	-30 05 58	1.06	-4.12	20.1	0.8	155.5±0.4	41.0±2.4	2.52±0.06	0.87
120-A	18 07 26.4	-29 39 34	1.76	-4.48	20.8	0.7	161.6±0.3	32.1±2.3	4.77±0.30	0.63
121-A	18 07 23.5	-30 32 55	0.957	-4.90	19.0	0.8	94.3±0.1	29.6±0.8	4.84±0.12	1.14
121-B ^v	18 09 36.0	-30 37 20	1.14	-5.35	19.9	0.7	219.2±0.2	16.4±0.9	3.23±0.08	2.20
124-A ^c	18 08 14.7	-30 57 48	0.70	-5.26	17.0	0.95	39.3±3.7	151.8±8.4	$3 \cdot 10^{11}$	2.92
124-B	18 07 51.9	-31 09 19	0.49	-5.28	20.0	0.7	168.4±0.2	33.9±0.4	$9 \cdot 10^{14}$	0.952
128-A	18 06 57.6	-29 00 55	2.28	-4.08	18.1	0.95	221.11±0.01	16.4±0.1	7.12±0.12	1.69
128-B ^c	18 07 18.6	-28 59 29	2.33	-4.13	16.4	0.95	143.8±0.1	30.7±0.3	2.18±0.02	3.84
159-A	18 17 04.7	-25 49 07	6.17	-4.52	18.2	0.7	89.9±6.2	21.9±6.7	1.61±0.49	0.83
159-B	18 18 08.0	-25 46 46	6.31	-4.72	20.8	0.7	130.9±0.1	66.7±3.9	8.57±0.36	1.38
162-A	18 16 44.3	-26 09 25	5.83	-4.62	17.2	0.7	145.5±0.1	21.9±0.4	2.38±0.06	2.95
162-B	18 14 59.7	-26 36 48	5.24	-4.49	19.9	0.8	211.0±0.8	36.2±3.8	2.09±0.09	0.71
167-A	18 13 32.1	-26 31 10	5.17	-4.16	20.1	0.95	107.5±0.3	32.4±2.0	3.03±0.08	0.73

Table 1: Parameters of the events. Column 1 indicates the label for each event with begins with its 3-digit field number. Columns 4 & 5 show the galactic longitude and latitude of the events, and Columns 6 & 7 show the approximate magnitude and color of the lensed stars. Columns 8-10 show the parameters of the best-fit microlensing models: time of peak amplification (Julian days–2449000), the event duration \hat{t} , and the peak amplification factor. Column 11 is the χ^2 per degree of freedom for the microlensing fit. The superscripts on the event labels denote various special features of the stars. Stars classified as clump giants are denoted with ^a, and the two exotic “parallax” and binary microlensing events are denoted with ^p and ^b, respectively. The two events also seen by the OGLE collaboration are labeled with ^o. Two likely microlensing events which fail our final cuts are denoted with ^f, while ^v and ⁿ indicate events which pass our cuts but are likely to be a variable star and a close neighbor of a variable star rather than microlensing.

Bulge Microlensing Optical Depth Estimates $\times 10^6$

cut	$\langle \ell \rangle$	$\langle b \rangle$	N	Confidence Levels						
				0.025	0.05	0.16	estimated	0.84	0.95	0.975
All stars (corr)	2.70	-4.08	41	1.57	1.69	1.98	2.43	2.97	3.33	3.52
“Clump Giant”	2.55	-3.64	13	1.60	1.90	2.66	3.92	5.79	7.09	7.75
“Clump Giant”, $ b < 3.5$	2.18	-2.95	10	2.21	2.75	4.07	6.32	9.89	12.32	13.59
“Clump Giant”, $ b > 3.5$	2.88	-4.33	3	0.31	0.44	0.80	1.57	3.21	4.59	5.35

Table 2: Microlensing optical depth estimates and confidence intervals. The first column shows the subsample of stars used. Columns 2–4 show the mean galactic latitude and longitude, and the number of events in the subsample. Columns 5–11 show the various confidence levels on the optical depth, as described in the text.

